Modeling of hydrogen ground state rotational and vibrational temperatures in kinetic plasmas

D.R. Farley *, D.P. Stotler, D.P. Lundberg, S.A. Cohen

Princeton Plasma Physics Laboratory, P.O. Box 451, Princeton, NJ 08543, USA

A B S T R A C T

A dipole-quadrupole electron-impact excitation model, consistent with molecular symmetry rules, is presented to fit ro-vibronic spectra of the hydrogen Fulcher-α Q-branch line emissions for passively measuring the rotational temperature of hydrogen neutral molecules in kinetic plasmas with the coronal equilibrium approximation. A quasi-rotational temperature and quadrupole contribution factor are adjustable parameters in the model. Quadrupole excitation is possible due to a violation of the 1st Born approximation for low to medium energy electrons (up to several hundred eV). The Born–Oppenheimer and Franck–Condon approximations are implicitly shown to hold. A quadrupole contribution of 10% is shown to fit experimental data at several temperatures from different experiments with electron energies from several to 100 eV. A convenient chart is produced to graphically determine the vibrational temperature of the hydrogen molecules from diagonal band intensities, if the ground state distribution is Boltzmann. Hydrogen vibrational modes are long-lived, surviving up to thousands of wall collisions, consistent with multiple other molecular dynamics computational results. The importance of inter-molecular collisions during a plasma pulse is also discussed.

© 2010 Elsevier Ltd. All rights reserved.

1. Introduction

Hydrogen is the most abundant and simplest element in the universe. Despite its simplicity and exact analytical solutions for atomic hydrogen's quantum mechanical wave functions, the spectroscopy of atomic and molecular hydrogen is complex. Spectroscopic lines are closely spaced and energy levels are often mutually perturbed.

Due to its relevance towards realizing fusion reactors, understanding the hydrogen states in plasma experiments is critical. The Princeton Field-Reversed Configuration (PFRC) device [1,2] operating at the Princeton Plasma Physics Laboratory is a compact toroid concept being pursued as an innovative approach towards a realizable fusion-energy reactor. To benchmark recent simulations of FRC behavior, detailed measurements of the molecular and atomic states of the PFRC hydrogen plasma are needed. Desired quantities are molecular and atomic hydrogen temperatures and densities. Also, molecular-assisted recombination (MAR), which depends on H_2 temperature, can have important effects on fusion plasma experiments [3]. Negative hydrogen ion sources (H^-) are also of significant interest due to their use in neutral beam devices for fusion research, and are produced through the dissociative attachment reaction which depends strongly on the internal energy state of neutral hydrogen molecules [4–6].

Industrial applications such as thin film deposition, in particular diamond deposition [7], which utilizes hydrogen plasmas, requires an understanding of chemical kinetics, which in turn requires knowledge of the internal energies of hydrogen. Another area of applicability is the charge-exchange reaction of protons with H_2, an endothermic reaction which is greatly enhanced by the internal energy of the H_2 molecule [8,9].

Doppler widths of molecular hydrogen emission lines could potentially be used to estimate H_2 translational

* Corresponding author. Tel.: +1 925 422 8110; fax: +1 925 422 0327.
E-mail addresses: farley2@llnl.gov, drfarley@aol.com (D.R. Farley).

temperature, but these widths are just ∼0.1 Å for applicable temperatures (up to 0.1 eV), while the PFRC experiment monochromator instrument linewidth is ∼0.7 Å, introducing intolerably large temperature uncertainties. Active probing of the plasma is often not advisable due to inducing plasma perturbations or melting the probe in energetic plasmas, and laser techniques are complicated and expensive. Other means of non-invasively measuring the internal energies of hydrogen are desirable.

Rotational temperatures obtained from rotational spectra may often be correlated with the neutral gas temperature since rotational and translational modes for most molecules equilibrate within 3–20 inter-molecular collisions [10]. However, hydrogen requires an anomalously large number of inter-molecular collisions (∼300) for rotational and translational modes to equilibrate at normal temperatures (∼200 for deuterium) [10,11]. Since inter-molecular collisions are infrequent in low-pressure kinetic plasmas, combined with their relative ineffectiveness at equilibrating hydrogen's rotational and translational modes, a direct measurement of gas temperature from rotational spectra may not be possible. Unfortunately, it is found that no correlation between rotational temperature and gas temperature can be made for the PFRC due to the low number of collisions within a plasma pulse, as will be detailed below. However, the purpose of this paper is directed towards quantifying the rotational and vibrational level populations resulting from the competing effects of electron-impact excitation and wall collision processes, regardless of whether the estimated rotational and vibrational distributions can be used as a gas temperature diagnostic.

The H_2 Fulcher-α emission ($d\ ^3\Pi_u \rightarrow a\ ^3\Sigma_g^+$) between 600 and 640 nm will be studied. The vibronic levels (electronic and vibrational) depicting the Fulcher-α excitation and emission processes are shown in Fig. 1. In this system, plasma electrons impact the ($X\ ^1\Sigma_g^+$) electronic ground state of hydrogen molecules, causing a spin-exchange collision to excite the ($d\ ^3\Pi_u$) electronic state, as well as exciting vibrational and rotational modes. Through analysis of the distribution of rotational lines and vibrational bands of the Fulcher-α emission, rotational and vibrational temperatures can potentially be obtained. The technique is passive in the sense that internal plasma electrons excite the molecules and the resulting emission is passively observed. Two main issues must be resolved to appropriately utilize this ro-vibronic emission to estimate the temperatures: (1) whether the ambient vibrational and rotational levels of the hydrogen gas follow Boltzmann distributions and (2) whether optical or non-optical selection rules should be used in modeling the electron-impact excitation process from the ground to excited states (optical rules are assumed for the radiative emission process). Note that the terminology *optical* transitions is equivalent to *dipole* transitions, and *non-optical* transitions, sometimes called *forbidden* transitions, would therefore include higher order multi-poles.

A cryogenically cooled (LN2) copper "test" cylinder was built and inserted into the PFRC chamber to test several spectroscopic models. The outer wall temperature of the cylinder was monitored by several thermocouples. Spectra
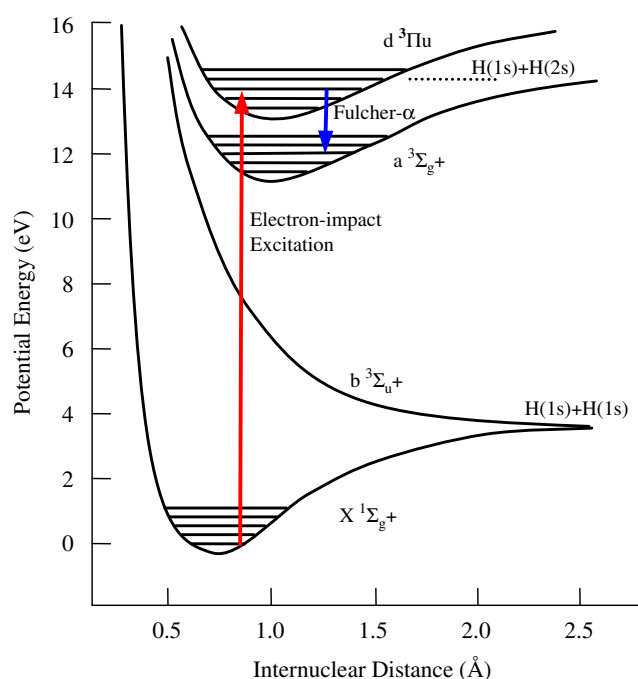

Fig. 1. Energy level diagram for relevant hydrogen electronic and vibrational states of the Fulcher-α system.

were obtained through collection of photons emanating from the interior of this cylinder at varying temperatures. In the following, time scales, electron-impact excitation, and wall collision effects are considered. A quantum mechanical formulation accounts for dipole as well as multi-pole transitions due to electron-impact excitation to the ($d\ ^3\Pi_u^-$) rotational states. Justification is made for using non-optical selection rules for electron-impact excitation modeling for electron energies below several hundred electron-Volts due to a violation of the 1st Born approximation [12]. An exact dipole-quadrupole spectroscopic model with adjustable temperature and quadrupole contribution parameters will be derived, which is simpler than other multi-pole formulations and fits experimental data better with a 10% quadrupole contribution.

Considerable discrepancies exist in the literature regarding electron-impact excitation mechanisms, the use of the 1st Born and Born–Oppenheimer approximations, ground state distribution considerations, collisions and wall effects, and molecular spectroscopic selection rules applied to hydrogen in low-pressure plasmas. As such, a comprehensive approach is taken here to clear up these issues, thus providing in one article a compendium of needed understanding to quantify internal energy temperatures of the hydrogen molecule from spectral measurements.

2. Spectroscopic background and assumptions

2.1. Ro-vibronic states of molecular hydrogen

In the PFRC, medium energy electrons (∼100–200 eV) generated by odd-parity rotating magnetic field (RMF$_0$) plasma heating [1], inelastically impact ground state H_2 ($X\ ^1\Sigma_g^+$) molecules exciting a proportion of them to the ($d\ ^3\Pi_u$) excited electronic state and ro-vibrational levels,

concurrently with changing the two-electron spin state from anti-parallel to parallel ($\uparrow\downarrow$ to $\uparrow\uparrow$).

As shown in Fig. 1, the dissociation limit to H(1s) and H(2s) lies between upper state vibrational levels $v' = 3$ and 4, such that the Fulcher-α emission from $v' \geq 4$ becomes considerably weak compared with other bands [13]. As such, only the $v' = 0$, 1, 2 and 3 diagonal bands will be considered. Note that a single prime will be used to refer to the upper states of the Fulcher-α system (d $^3\Pi_u$), no prime for the ground states (X $^1\Sigma_g^+$), and two primes for the final states (a $^3\Sigma_g^+$). The vibrational energy levels of each electronic state e are given by [14]

$$G_e(v) = \varpi_e\left(v + \frac{1}{2}\right) - \varpi_e x_e\left(v + \frac{1}{2}\right)^2 \qquad (1)$$

where ϖ_e is the equilibrium vibrational frequency, and x_e is a second-order correction factor. The rotational energy levels within a given vibrational band (neglecting centrifugal correction constant D_v) are

$$F_e(N) = B_v N(N+1) \qquad (2)$$

where N is the rotational quantum number, and $B_v = B_e - \alpha_e(v+1/2)$ is the rotational constant for vibrational state v. The values for the vibrational parameters and rotational constants are provided in Table 1.

The total energy of ro-vibronic levels is given by

$$E_e(v,N) = T_e + G_e(v) + F_e(v,N) \qquad (3)$$

where T_e is the energy of the electronic states. Using Eqs. (1)–(3), the wavelengths for the Fulcher-α rotational lines can be calculated, as summarized in Table 2 for the Q-branch lines ($\Delta N = 0$) for $N' = 1 \rightarrow 5$. Note that hyperfine (nuclear spin–electron orbit coupling) and triplet splitting is very small for H_2, such that each ro-vibronic line can be considered a singlet for the present purposes.

2.2. Molecular symmetry

It will be useful to review angular momentum coupling of diatomic molecules of the Hund's case (b) type [14]. As shown in Fig. 2, R is the angular momentum vector for the rotating molecule. Angular momentum N is the vector sum of Λ and R, where Λ is the projection of electron orbital angular momentum along the inter-nuclear axis, which equals 0 for Σ electronic states and 1 for Π electronic states. Note that $\Sigma^{\pm}$ or $\Pi^{\pm}$ electronic state parities refer to the reflection symmetry through a plane passing through the inter-nuclear axis (+ denotes no change in sign of the electronic eigenfunction; $-$ denotes a change in sign). For Hund's case (b) molecules, quantum number N is the "good" quantum number to be used in calculating rotational

energies, rather than J which includes the electron spin vector S. The Hund's case (b) assumption is always true for Σ states, and the hydrogen $^3\Pi$ state can also be considered case (b) due its very small spin–orbit coupling constant (0.0281 cm$^{-1} \ll B_e = 30.364$ cm^{-1}). M is the projection of J on the axis collinear with an applied magnetic field B, same as defined for atomic spectroscopy. Without an applied field, a rotational state is degenerate by $(2J+1)$ or equivalently $(2N+1)(2S+1)$.

A rotational level is termed "positive" or "negative" depending on whether the molecular total eigenfunction (not just rotational eigenfunction) remains unchanged or changes sign upon reflection at the origin, respectively. The selection rule is $+ \leftrightarrow -$. For homonuclear molecules such as hydrogen, the exchange of nuclei cause the total eigenfunction to either remain unchanged (symmetric) or changes sign (anti-symmetric) with selection rules symmetric $\leftrightarrow$ symmetric, anti-symmetric $\leftrightarrow$ anti-symmetric. These selection rules hold for radiative transitions as well as collisional transitions. Rotational levels will be positive or negative, symmetric or anti-symmetric, depending on whether the rotational quantum number N is even or odd

Table 2
Wavelengths (nm) of Q-branch lines of Fulcher-α diagonal vibrational bands.

(v',v'')	Q1	Q2	Q3	Q4	Q5
(0,0)	601.84	602.39	603.22	604.32	605.71
(1,1)	612.25	612.80	613.62	614.73	616.12
(2,2)	622.60	623.15	623.97	625.08	626.46
(3,3)	632.87	633.42	634.24	635.34	636.72
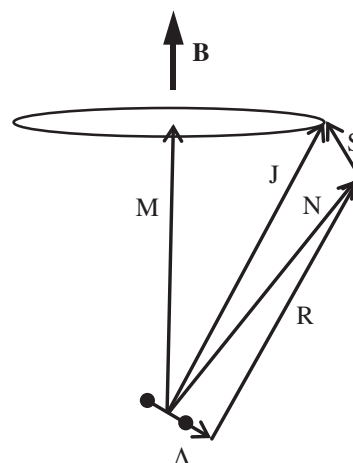
Fig. 2. Coupling of angular momentum vectors in the presence of magnetic field B for Hund's case (b) diatomic molecules.

Table 1
Molecular constants for H_2 ground state and Fulcher-α electronic states.

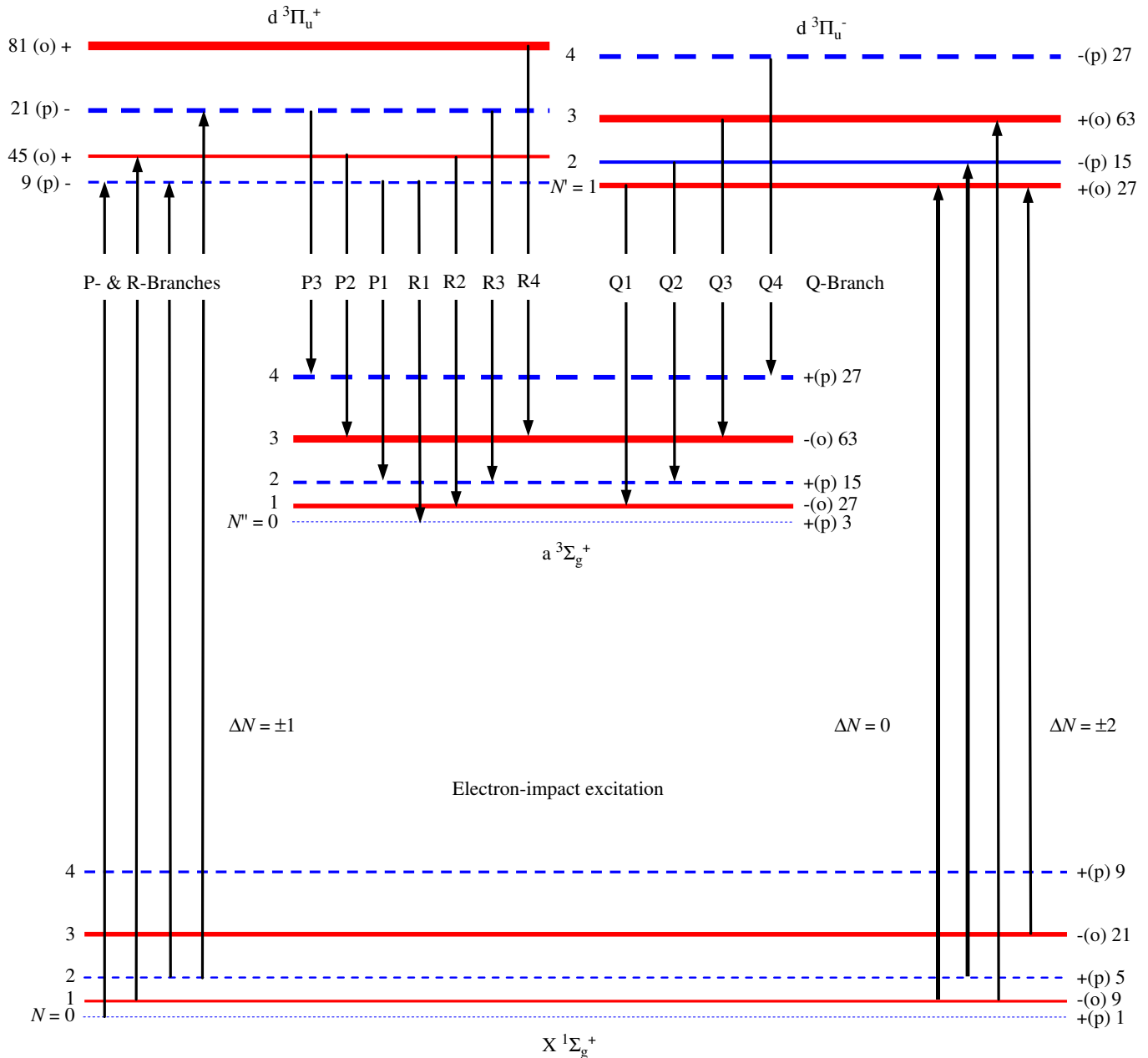| State	T_e (cm^{-1})	ϖ_e (cm^{-1})	$\varpi_e x_e$ (cm^{-1})	B_e (cm^{-1})	α_e (cm^{-1})	r_e ($\times 10^{-8}$ cm)
d $^3\Pi_u$	112,702	2371.58	66.27	30.364	1.545	1.0496
a $^3\Sigma_g^+$	95,938	2664.83	71.65	34.216	1.671	0.9887
X $^1\Sigma_g^+$	0	4395.2	117.99	60.809	2.993	0.7416

Herzberg [14].

Fig. 3. Rotational level diagram for the H_2 molecule and its Fulcher-α emission.

(or vice versa). Shown in Fig. 3 is the rotational energy diagram for electron-impact excitation of X $^1\Sigma_g^+ \rightarrow$ d $^3\Pi_u$ and Fulcher-α emission (d $^3\Pi_u \rightarrow$ a $^3\Sigma_g^+$). Positive rotational levels are denoted with a plus sign, and negative with a minus sign. Note that Λ-doubling causes the rotational lines to shift to slightly higher energy with increasing N for the Π^+ electronic state symmetry versus the Π^- electronic state symmetry, as shown in Fig. 3.

A proton has nuclear spin 1/2. Since molecular hydrogen has two protons, the total spin L equals 1 (parallel spins) or 0 (anti-parallel spins). The rotational levels therefore have statistical weight $2L+1$, such that the weight of odd/even-numbered rotational lines is 3:1. Actually, however, nuclear spin causes very small splitting of the lines into multiplets, which is increased with an applied magnetic field, but usually the splitting is so small that it is ignored

and considered a single level with statistical weight $2L+1$. For the ground state of H_2, even-numbered rotational levels are positive/symmetric with anti-parallel proton spins ($L=0$), while odd levels are negative/anti-symmetric with parallel spins ($L=1$). For homonuclear molecules with non-zero total nuclear spin ($L>0$), the selection rules s $\leftrightarrow$ s and a $\leftrightarrow$ a do not strictly hold, but it could take months or years for a molecule to go from an even-numbered to odd-numbered rotational level. As a result, gases such as ground state H_2 may be regarded as a mixture of two modifications—a symmetrical with only even-numbered rotational levels, and an anti-symmetrical with only odd-numbered symmetrical levels. The modification with the greater statistical weight ($2L+1$) is called the *ortho* modification, while the lower weight is called the *para* modification. There is a one-to-one correspondence between

nuclei inversion and nuclear spin symmetries such that for all hydrogen ro-vibronic levels the *para* modification is always symmetrical, while the *ortho* modification is always anti-symmetrical. As such, it is sufficient to denote rotational levels with just + or −, and (p) or (o) for *para* and *ortho* modifications, respectively. This nomenclature is used in Fig. 3. Blue (dashed) lines are always the *para* (symmetric) modification, and red (solid) lines are the *ortho* (anti-symmetric) modification. Also shown along with the rotational level symmetry is its statistical weight equal to $(2L+1)(2N+1)(2S+1)$, with the thickness of each line scaled to this statistical weight. Note that each of the contributions to the total degenerate line has the same symmetry (+ or −, *para* or *ortho*) such that the selection rules still hold for these degenerate components.

It is important to carefully examine the symmetries and selection rules for hydrogen's rotational levels. As shown in Fig. 3, *para* states only transition to other *para* states, and similar for *ortho* states, and always from + to − or vice versa. This leads to the result that Q-branch rotational emissions ($\Delta N = N' - N'' = 0$) must come from the Π^- parity of the upper state, while R- and P-branch emissions ($\Delta N = N' - N'' = \pm 1$, respectively) decay from the Π^+ parity. Further, electron-impact excitation can only change the rotational quantum number N by an even number (i.e. $\Delta N = N' - N = 0, \pm 2, \pm 4$, etc.) if exciting to the Π^- state, while the change in N must be odd for exciting the Π^+ state (i.e. $\Delta N = \pm 1, \pm 3$, etc.). Because $|\Delta N| > 2$ transitions are generally relatively weak, examples of these otherwise allowed larger transitions are not shown in Fig. 3. The $\Delta N = 0$ transitions are the strongest, and are shown as thicker lines in Fig. 3.

2.3. Optical and non-optical selection rules

As described by Otorbaev [15], there has been considerable debate as to the effect an impacting low-mass electron can have on a much more massive body such as a H_2 molecule. It has sometimes been assumed that the low mass of the electron can have no effect on the rotational state of the molecule [14,16,17], hence that $\Delta N = N' - N = 0$ for electron-impact excitation. The benefit of assuming $\Delta N = 0$, if such an assumption could be justified, is that the rotational distribution of the ground electronic state can then be assumed to be directly "imaged" or "mapped" into the upper excited state. An "excitation" rotational temperature is measured using a traditional Boltzmann plot, assuming the ratio T_r/B_v is maintained (see Eq. (2)), where T_r is the rotational temperature. The measured upper state rotational temperature is related to the ground state rotational temperature through $T_r = B_v T'_r / B'_v$, where again the prime denotes the upper state and no prime is the ground state. For the hydrogen Fulcher-α electronic states, this equates to $T_r \approx 2 T'_r$ (see Table 1), and so the $\Delta N = 0$ assumption leads to the ground state rotational temperature being twice the rotational temperature of the upper state. Note, however, that this concept of an "excitation" temperature is unnecessary and confusing. If the ground state rotational temperature is properly followed through the analysis, as is done below, then there is no need for such an excitation temperature. Also, measuring an upper state

rotational temperature insinuates that the upper states have achieved an equilibrium amongst themselves (i.e. through collisions), which for the rapid radiative times of the upper state is doubtful. While the ground state distribution is preserved for dipole (if higher rank multipoles are presumed not necessary) electron-impact excitation and Q-branch emission, this direct mapping is not the same as actual upper state equilibration.

Due to symmetry requirements as described in the previous section, if the $\Delta N = 0$ electron-impact excitation criterion were strictly true, then there would be no P- or R-branch transitions from the Fulcher-α emission. These branches have been observed, [18] although the (d $^3\Pi_u^+$) parity electronic state is known to be perturbed strongly by the (e $^3\Sigma_u^+$) state [19,20], so the P- and R-branches are not normally used, regardless [21]. Further, in a cryogenically cooled hydrogen discharge experiment [22], whereby only the first ground state rotational level is expected to be populated, a full rotational distribution of the upper rotational states (up to $N' = 6$) was produced from electron-impact excitation, which, by their reasoning, demonstrated that electrons can affect molecular rotation such that a strict $\Delta N = 0$ rule is not valid.

The ground state could have a non-equilibrium rotational distribution [16,23–26], such that the assumption that all molecules are in the lowest rotational ground state as used in Ref. [22] may be inadequate. Primary electron impact or secondary effects (e.g. chemical reactions, collisions with ions or vibrationally excited molecules, cascade processes, secondary electrons) can alter the ground state distribution. If inter-molecular or wall collisions are insufficient to re-establish equilibrium with the background gas or wall temperature before the molecules are excited to the (d $^3\Pi_u$) upper electronic state through an electron-exchange impact transition, then a Boltzmann rotational distribution is not justified. This was the argument of Lavrov et al. [23] to dispute the results of Otorbaev et al. [22], although the initial results of Lavrov et al. [27] determined that optical selection rules were appropriate for the excitation of hydrogen, thus agreeing in effect with Otorbaev et al. [22] that electron impacts can affect H_2 internal modes.

Multiple studies [27–30] have assumed optical selection rules apply ($\Delta N = 0, \pm 1$) during electron-impact excitation. However, even if optical selection rules apply, symmetry requirements lead to $\Delta N = 0$ only for the X $^1\Sigma_g^+ \rightarrow$ d $^3\Pi_u^-$ parity electron-impact excitation process (i.e. Q-branch excitation), and $\Delta N = \pm 1$ for the X $^1\Sigma_g^+ \rightarrow$ d $^3\Pi_u^+$ parity excitation (i.e. R- and P-branch excitations), resulting again in Q-branch Fulcher-α line emissions being a direct image of the ground state rotational distribution. Optical selection rules, therefore, are effectively equivalent to the premise that the electron-impact excitation process preserves the ground state rotational distribution, if just Q-branch emissions are to be observed. Similarly, Bryukhovetskiy et al. [31] derived the *approximate* selection rule $\Delta N \leq |A' - A|$, which yet again corresponds to $\Delta N = 0, \pm 1$ for X $^1\Sigma_g^+ \rightarrow$ d $^3\Pi_u$, which implicitly corroborates the assumption of optical selection rules.

Non-optical selection rules would violate this concept of direct mapping of rotational distributions. Bryukhovetskiy

et al. [31] used multi-pole transition moments in modeling experimental electron-impact excitation data, and empirically determined that quadrupole excitation is not so small, with contributions as high as 20% of dipole probabilities in some cases (see Table 5). To understand whether optical or non-optical selection rules should apply, it is necessary to review the 1st Born approximation for electron scattering.

2.4. The 1st Born and Born–Oppenheimer approximations

The form of the solution for the total wave function representing the scattering of an electron beam moving in the z-direction by a scattering center with potential $V(r)$ is [32]

$$\psi \sim e^{ikz} - \frac{e^{ikr}}{r}\frac{1}{4\pi}\int e^{-ik\overrightarrow{n}\cdot\overrightarrow{r}'}V(r')\psi(r')d\zeta' \qquad (4)$$

where k is the wavenumber of the incident electron wave, r is the radial direction from the scattering center, $\overrightarrow{n}$ is a unit vector in the direction of the scattered electron, and $d\zeta'$ is a small volume around r'. Eq. (4) is exact. Physically, this equation describes an outgoing plane wave of the original electron beam plus a quasi-spherical wave caused by the scattering event. To solve this equation, Born [12] assumed that the final wave function is not much different from the wave function of the incoming incident electrons *if they are fast*, such that $\psi(r') \rightarrow e^{ikz'}$ in the integral of Eq. (4). Using this substitution, the wave function of the scattered event is then easily solved, which provides directly a differential cross section as the square of the integral term in Eq. (4) [32]. Oppenheimer [33] expanded upon this work of Born, identifying that impacting and atomic bound electrons should be considered indistinguishable, providing a similar means to calculate the differential cross section for electron-exchange reactions. Unfortunately, this method of calculating the differential cross section, where the incident wave function is assumed to be rather unaffected by the scattering event, is sometimes called the "Born and Oppenheimer" approximation [34,35], which causes confusion with the other more familiar Born–Oppenheimer approximation [36] that allows for the separation of electronic and nuclear (vibration and rotation) wave functions. To avoid this confusion, we will use the terminology *1st Born approximation* to denote the assumption of using the incident high-speed electron wave function in the scattering integral for fast electrons; and the *Born–Oppenheimer approximation* to denote the assumption of separable electronic and nuclear components of the total wave function.

Proceeding along these lines, for the 1st Born approximation to be applicable the incident electrons must be fast. For hydrogen molecules as the scatterer, it was found that the approximation fails badly for electron energies below about 100 eV [35]. For atomic hydrogen, the approximation breaks down for impact energies significantly lower than 50 times the excitation energy [37], which means that an order of 100's eV are required to satisfy the 1st Born approximation for atomic hydrogen. This order of magnitude is also consistent with helium results [32]. All of the hydrogen experiments cited above [15–17,23–31] had electron energies far below 100's of eV, more typically

from several eV to 100 eV, such that the 1st Born approximation should not have been be considered valid in those studies. The PFRC has electron temperatures of 100–200 eV, so the 1st Born approximation will not be assumed in this study.

A consequence of violating the 1st Born approximation is that non-optical selection rules become more probable than otherwise. Following the results of electron scattering by atoms, the cross section for excitation of atomic hydrogen from states 1 to 2 is given by [38]

$$\sigma_{12} = \frac{4P_2}{P_1(\Delta P)^2}\Big[\varepsilon_1^2 + (\varepsilon_2^2 - 2\varepsilon_1\varepsilon_2)(\Delta P)^2$$
$$+ (\varepsilon_3^2 - 2\varepsilon_2\varepsilon_4 + 2\varepsilon_1^2\varepsilon_5)(\Delta P)^4 + \cdots\Big] \qquad (5)$$

where P_1 and P_2 are the incoming and outgoing momenta of the incident electron, respectively, ΔP is the magnitude of the vector difference of these momenta ($\Delta P^2 = P_1^2 + P_2^2 - 2P_1P_2\cos\vartheta$, where ϑ is the angle between vectors P_1 and P_2), and ε_k is the multipole moment of rank k. Hartree atomic units are used in Eq. (5). The multi-poles are given by

$$\varepsilon_k = \frac{1}{k!}\sum_s \int z_s^k \psi_1\psi_2^* \qquad (6)$$

where the sum is over s bound electrons of the atom and z is the spatial coordinate. It is clear from Eq. (6) that ε_1 is the dipole moment, ε_2 is the quadrupole moment, etc.

From Eq. (5) it is evident that for small changes in the incident electron momentum ($\Delta P \ll 1$), the scattering cross section is dominated by dipole (optical) transitions. However, if ΔP is not small, then higher rank multi-pole moments can become important such that non-optical transitions may have non-negligible probability. This is the essence of the 1st Born approximation since high-speed incident electrons lose little energy in the scattering event, and experience small scattering angles. For the PFRC hydrogen plasma with ∼100–200 eV electrons, therefore, both optical and non-optical excitation rates should be considered. Note that other researchers [39–41] used keV electron beams as a temperature diagnostic applied to rarefied gas dynamic flows for gases other than hydrogen, correctly recognizing that high electron energies were needed.

The Franck–Condon (FC) principle is also often invoked in the spectroscopy of diatomic molecules to estimate vibrational branching ratios during excitation and emission. In the FC approximation, the vibrational wave functions are assumed to be separable from the other components of the total wave function, namely the electronic and rotational wave functions. Implementation of the FC approximation implicitly assumes the Born–Oppenheimer approximation is also valid. With the FC approximation, the inter-molecular distance is assumed fixed during an electronic or radiative transition, which are much faster processes than vibrational motion, such that vibrational modes image directly from one potential well to the other. The branching ratio, or Franck–Condon factor, is calculated by the overlap integral of the vibrational wave functions of the two states involved in the transition. The FC approximation also assumes there is no vibration-rotation interaction (i.e. the vibrational wave functions

do not depend on rotational quantum number N), which has been shown to be true for Q-branch *emission* of the H_2 Fulcher-α emission [42]. During electron-impact *excitation* of H_2, however, separation of the vibrational and rotational wave functions may not be valid. Alternative excitation models which include, and do not include, the FC approximation will be studied below.

3. Plasma parameters

3.1. PFRC experimental setup

A sketch of the PFRC is shown in Fig. 4. An 80-cm-long, 10-cm inner diameter Pyrex cylinder is the main vacuum vessel. Internal are six coaxial magnetic flux-conserving copper rings, three on each side of the midplane, separated from each other by 6–7 cm. (Experiments described in Ref. [1] used 10 flux conservers.) The flux conservers nearest the midplane have an ID of 8.3 cm; the outermost have IDs of 5.5 cm and the middle two 7.4 cm, roughly conforming to the shape of the vacuum field. External to the Pyrex vessel and symmetric about its midplane is the 28-cm-long, 2-turn RMF_o antenna, separated from the vessel by a Faraday shield. Typical RMF_o characteristics are: antenna current 150 A, field strength $B_R \sim 10$ G, and frequency $\omega_R/2\pi = 14$ MHz. An axial field of ~ 100 G is maintained at the FRC centerline, resulting in $90\omega_{ci} \approx \omega_R \approx \omega_{ce}/20$, where $\omega_c = qB_a/mc$ is the particle cyclotron frequency, m is the particle mass, q is the particle charge, and subscripts e and i refer to electrons and ions, respectively. A static mirror-configuration magnetic field is created by coaxial small-bore and large-bore coils located near $z = \pm 45$ cm and $z = \pm 105$ cm. Nominally, these coils produce an axial field of strength $B_a = 50$ G at axial location $z = 0$ cm and 5–6000 G at $z = \pm 45$ cm.

A picture of the 3(1/2) in long, 1(1/4) in inner diameter (1/8 in thick) copper test cylinder that was inserted into the PFRC vacuum chamber is shown in Fig. 5. The refrigerant copper tubing which circulates the liquid nitrogen wraps around the outside of the tube in a serpentine configuration, and was brazed in place. The thermocouple connections are also shown. Small optical access holes were drilled into the tube at the midplane and edge of the tube. The midplane hole was primarily used to ensure that as many wall collisions as possible occurred prior to observing the Fulcher-α emission.
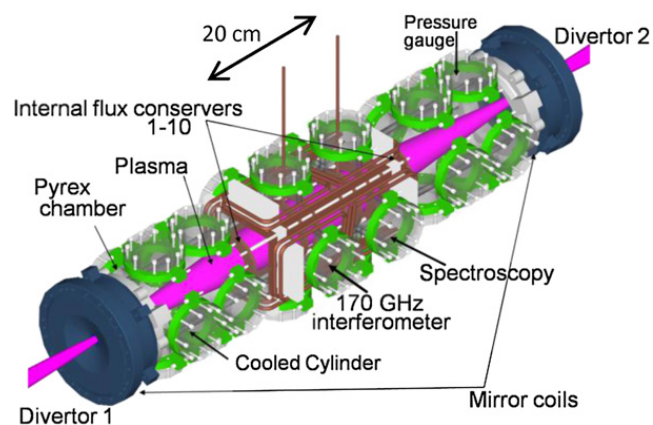

Fig. 5. Picture of the cryogenically cooled 3(1/2) in long, 1(1/4) in inner diameter (1/8 in thick) copper cylinder. The attached copper refrigerant tubing and optical access holes are shown. The interior is coated with graphene material Aquadag.

The edge access hole was used as a check to see if there was any indication of edge effects on the spectra. A thin layer of graphene material was painted on the interior of the cylinder to minimize reflection of light (the wall collision surface is carbon-based rather than copper, which alters the wall accommodation). The refrigerant tubing extends vertically to a lexan access port on top of the PFRC chamber, where a stainless steel coupler then attaches to the cryogenic feed system. Wall temperatures of ~ 92 K were achieved from thermocouple measurements on the test cylinder.

Optical fibers connected to compact lenses can be focused within the PFRC, and fed into a 0.5 m monochromator and associated intensified 26 μm pixel size CCD array. Three diffraction gratings are available (600, 1200 and 1800 grooves/mm). The 1800 groove grating were used for measuring rotational lines within a vibrational band, giving a pixel resolution of 0.2 Å in the 600–640 nm spectral range of interest. The fibers can be moved in the radial r-direction, such that spectroscopic measurements across the entire plasma diameter can be recorded. One such fiber was mounted on the bottom port near Diverter 1 in Fig. 4 to view the interior of a cryogenically cooled copper cylinder, which was placed within the chamber.

Hydrogen gas is continuously flowed through the PFRC vacuum chamber to maintain a pressure typically of ~ 1 mTorr. The H_2 gas temperature, for order of magnitude estimates of kinetic parameters, could be between room temperature and ~ 700 K, based on initial rotational temperature measurements. The H_2 thermal speed is thus $V_{H2} \sim 1.2\text{–}1.8 \times 10^5$ cm/s, and the H_2 density is $n_{H2} \sim 3 \times 10^{13}$ cm^{-3}. Dissociation of about 10% is assumed from previous experimental and computational estimates, giving an atomic hydrogen density of $n_H \sim 10^{12}$ cm^{-3}. The electron density is also about 10^{12} cm^{-3}.

3.2. The coronal approximation

The coronal equilibrium model is often assumed for low-density, optically thin plasma [43]. In the coronal

Fig. 4. Schematic of the Princeton FRC.

equilibrium approximation, electron-impact excitation is the primary means of populating upper states, and spontaneous emission is the primary de-population mechanism. Justification that the coronal approximation is valid should be done prior to developing a model which assumes electron-impact as the dominant excitation mechanism and spontaneous emission as the dominant de-population mechanism.

To estimate the populations of the electronic states, rate equations will be used. The rate of change in electronic state populations, assuming $E_1 < E_2 < E_3 \ldots$, is given by [43]

$$\frac{dn_i}{dt} = -\sum_{j<i}\left[n_i A_{ij} + n_i \rho(\overline{v}_{ij})B_{ij} - n_j \rho(\overline{v}_{ij})B_{ji}\right] + \sum_{j>i} n_j A_{ji}$$
$$-\sum_{i \neq j}\left[n_e n_i \langle \sigma_{ij}V_e \rangle - n_e n_j \langle \sigma_{ji}V_e \rangle\right] \qquad (7)$$

where n_i is the density of state i, A_{ij} is the Einstein emission coefficient for transitions from state i to j, B_{ij} is the Einstein stimulated emission coefficient, B_{ji} is the Einstein absorption coefficient, $\rho(\overline{v}_{ij})$ is the radiation density for photons with wavenumber $\overline{v}_{ij}$ (cm^{-1}), σ_{ij} is the collisional cross section for deactivation through electron impact, σ_{ji} is the cross section for electron-impact excitation, and V_e is the impacting electron average velocity. In Eq. (7), the second summation for $j > i$ is spontaneous emission for cascade transitions from states above state i. Excitation of molecular hydrogen by dissociated H atoms with energy of about 0.4–1 eV (obtained from Doppler broadening of the H$_\alpha$ line in the PFRC using a 0.5 m monochromator with associated CCD pixel resolution of ~ 0.2 Å) is negligibly small in comparison with electron-impact excitation of H$_2$. H$^+$ impact excitation of H$_2$ will similarly be neglected.

Assume a 4-level electronic state manifold for the Fulcher-α system as depicted in Fig. 6. Here, state $|4>$ represents all states above the (d $^3\Pi_u$) upper state of the Fulcher-α system, which includes other Σ, Π and Δ configurations in the $n=4$, 5, etc. levels. Since the intensity of the Fulcher-α emission depends directly on the (d $^3\Pi_u$)
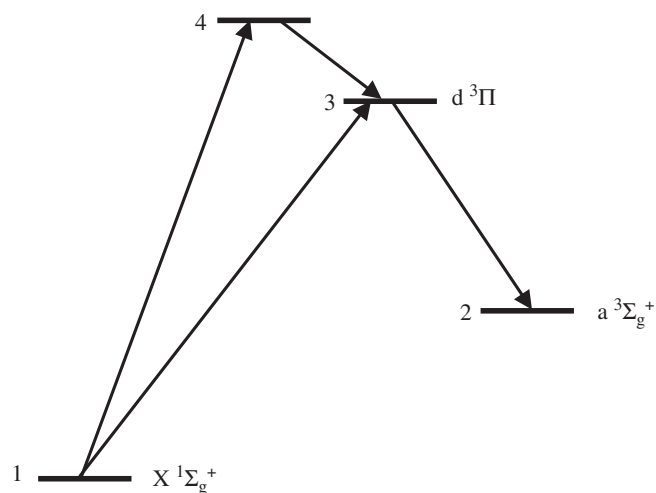

Fig. 6. Electronic state diagram for Fulcher-α system (H$_2$ $\times$ $^1\Sigma_g^+$ $\rightarrow$ d $^3\Pi_u$ $\rightarrow$ a $^3\Sigma_g^+$).

upper state population, n_3 will be analyzed using Eq. (7)

$$\frac{\dot{n}_3}{n_3} = -A_{31} - A_{32} - \rho(\overline{v}_{31})B_{31} - \rho(\overline{v}_{32})B_{32} + \frac{n_1}{n_3}\rho(\overline{v}_{31})B_{13}$$
$$+ \frac{n_2}{n_3}\rho(\overline{v}_{32})B_{23} + \frac{n_4}{n_3}A_{43} - n_e\langle\sigma_{31}V_e\rangle - n_e\langle\sigma_{32}V_e\rangle$$
$$- n_e\langle\sigma_{34}V_e\rangle + \frac{n_1}{n_3}n_e\langle\sigma_{13}V_e\rangle + \frac{n_2}{n_3}n_e\langle\sigma_{23}V_e\rangle$$
$$+ \frac{n_4}{n_3}n_e\langle\sigma_{43}V_e\rangle \qquad (8)$$

The A_{31} and B_{31} photon emission and absorption transitions are not allowed by spin selection rules ($\Delta S = 0$), so these terms will be ignored. The wavenumber difference between the $|4>$ and $|3>$ electron states is about 6000 cm^{-1}, and for the Fulcher-α $|3> \rightarrow |2>$ transition is 16,764 cm^{-1} (see Table 2 for electron energy levels E_e). Since spontaneous emission rates scale as the cube of wavenumber, A_{43} will be about 5% of A_{32}. If the electron-impact excitation rate to the $|4>$ state is similar to the $|3>$ state rate, and taking into account the n^2 degeneracy factor (~ 2) and assuming all the excited population from the $|4>$ state decays only to the $|3>$ state, the effect upon the $|3>$ state population would be $\sim 10\%$. Other experiments done in hydrogen at 40 mTorr and 35 eV estimated that the maximum total contribution of cascade transitions to the $^3\Pi_u$ electronic state is 17% [44]. Therefore, the A_{43} term in Eq. (8) will be ignored in contributing to the $|3>$ state population, tolerating up to $\sim 20\%$ error in the (d $^3\Pi_u$) population. For the collisional terms, the density ratio of $n_1/n_3 \gg 1$ (estimated to be several orders of magnitude) while the σ_{ij} and σ_{ji} cross section values are of the same order of magnitude, such that the $(n_1/n_3)n_e\langle\sigma_{13}V_e\rangle$ collisional rate overwhelms the other collisional terms in Eq. (8). With these assumptions, Eq. (8) reduces to

$$\frac{\dot{n}_3}{n_3} = -A_{32} - \rho(\overline{v}_{32})B_{32} + \frac{n_2}{n_3}\rho(\overline{v}_{32})B_{23} + \frac{n_1}{n_3}n_e\langle\sigma_{13}V_e\rangle \qquad (9)$$

As will be justified below, the Fulcher-α emission in the PFRC plasma is optically thin, so the absorption and stimulated emission terms can be neglected. The (d $^3\Pi_u$) electronic state decays primarily to the (a $^3\Sigma_g$) state, such that we can denote the total emission time $\tau = \tau_{em} = 1/A_{32}$, and Eq. (9) can be written as

$$\frac{\dot{n}_3}{n_3} = -1/\tau_{em} + \frac{n_1}{n_3}n_e\langle\sigma_{13}V_e\rangle \qquad (10)$$

Eq. (10) is not valid in regions within the PFRC vacuum chamber where there are few electrons, such as outside the magnetic flux conserver coils. The collision term in Eq. (10) should then be neglected, such that Eq. (10) simplifies to simple radiative decay of the (a $^3\Pi_u$) population in these regions.

In steady state, the population of the H$_2$ (d $^3\Pi$) electronic state is thus given by

$$n_3 = n_1 n_e \langle\sigma_{13}V_e\rangle \tau_{em} \qquad (11)$$

Eq. (11) is identified as the coronal equilibrium model. The excitation cross section σ_{13} is approximately 7×10^{-17} cm^2 [45] and with an electron temperature of ~ 100–200 eV, $n_e \sim 10^{12}$, $n_1 \sim 3 \times 10^{13}$ and $\tau_{em} \sim 40$ ns [46] in Eq. (11), the upper state population for H$_2$ d $^3\Pi_u$ is $n_3 \sim 4 \times 10^{10}$ cm^{-3}. Also from these parameters, the electron-impact excitation rate

$n_e \langle \sigma_{13} V_e \rangle$ equals $\sim 3 \times 10^4 \, \mathrm{s}^{-1}$, corresponding to an excitation time scale of $\tau_{ex} \sim 30 \, \mu\mathrm{s}$.

The same procedure as above can be used to estimate the population of the n_2 (a $^3\Sigma_g^+$) state. However, in this case the cascade transitions from the (d $^3\Pi_u$) to (a $^3\Sigma_g^+$) states should not be ignored, while other cascade transitions as well as absorption and stimulated emission will again be neglected. The rate equation for the (a $^3\Sigma_g^+$) state is then

$$\dot{n}_2 = -n_2 A_{21} + n_3 A_{32} + n_1 n_e \langle \sigma_{12} V_e \rangle \qquad (12)$$

In steady state, $n_2 = (n_3 A_{32} + n_1 n_e \langle \sigma_{12} V_e \rangle)/A_{21} \cong n_3 A_{32}/A_{21}$ since the cross section σ_{12} at 100 eV is small at $\sim 10^{-19} \, \mathrm{cm}^2$ [47,48], such that the collisional term is negligible in comparison with the A_{32} spontaneous emission rate. The emission time of the n_2 state ($1/A_{21}$) is 10 ns [49,50], resulting in a population of the (a $^3\Sigma_g^+$) state of $\sim 10^{10} \, \mathrm{cm}^{-3}$, similar to the population of the (d $^3\Pi_u$) state.

The optical depth δ can be approximated, assuming Doppler broadening exceeds natural line broadening, through $\delta(\lambda) \approx 1.8 \times 10^{-13} n_2 \lambda l \sqrt{m_A c^2 / k_B T_{gas}}$, where m_A is the atomic mass, k_B is the Boltzmann constant, λ is the line radiation wavelength, and l is the distance propagated within the gas (cgs units) [51]. Assuming room temperature gas and a characteristic length of 10 cm, the resulting optical depth for the Fulcher-α emission is much less than 1 such that the emission can be considered optically thin. This further validates the use of the coronal equilibrium model. Note that other emissions, such as the ultraviolet Werner and Lyman bands (C $^1\Pi_u \rightarrow {}^1\Sigma_g^+$ and B $^1\Sigma_u^+ \rightarrow {}^1\Sigma_g^+$, respectively) are optically thick in this plasma, so could affect the ground state electronic population. However, this would not alter the conclusion that the coronal approximation is valid for the subsequent modeling derivation.

3.3. Time scales

At probable PFRC gas temperatures of 300–700 K, the H_2 thermal speed is 1.2–1.8×10^5 cm/s. The H_2 mean free path ($k T_{gas}/\pi\sqrt{2}pd^2$) [52], with the H_2 hard sphere diameter $d = 2.71 \times 10^{-8}$ cm and pressure $p \sim 1$ mTorr, is of the order 10–20 cm for PFRC conditions, resulting in a time interval between molecular collisions of $\tau_{coll} \sim 100 \, \mu\mathrm{s}$ (10 kHz). However, the vacuum vessel has a diameter of 10 cm, and there are multiple copper flux conservers within the chamber, so hydrogen molecules have a slightly higher probability of colliding with wall structures rather than collisions with each other. In this sense, the PFRC plasma is in the kinetic regime. The copper test cylinder has an inner diameter of 3.2 cm, resulting in a wall collision frequency of 30 kHz, three times greater than collisions with the vacuum chamber wall.

X-ray pin-diode measurements have revealed that the PFRC plasma electron-energy distribution has a non-Maxwellian high-energy tail. The effect of high energy tails of the electron velocity distribution will not alter the electron-impact excitation time scale of $\tau_{ex} \sim 30 \, \mu\mathrm{s}$ calculated in the previous section, assuming the number density of the higher energy electrons decrease exponentially with energy, whereas the increased collision rate scales as $V_e \sim E^{1/2}$. Therefore, higher energy tail electrons will not be effective at increasing the electron-impact collision rate.

Note also that 100 eV electron-impact, spin-exchange excitation removes impacted molecules from the ground state population, which do not re-enter the X $^1\Sigma_g^+$ ground electronic state prior to emitting their fluorescence (triplet spin states do not mix with singlet states). Thus, the electron-impact excitation rate does not directly affect the ground state distributions, although recycled neutrals from the walls eventually return to the ground electronic state population.

Shown in Table 3 are the plasma pulse duration τ_p (~ 3 ms), inter-molecular collision time τ_{coll}, wall collision times for the PFRC chamber and within the test cylinder, $(\tau_{wall})^{PFRC}$ and $(\tau_{wall})^{TEST}$, respectively, the upper Fulcher-α state (d $^3\Pi_u^-$) emission time τ_{em}, the lower Fulcher-α state (a $^3\Sigma_g^+$) emission time $\tau_2 = 1/A_{21}$, and the electron-impact excitation time τ_{ex}. All time scales are listed with just one significant digit for an order of magnitude comparison. The following picture of the processes affecting the PFRC H_2 molecules emerges from examination of Table 3. Radiative processes occur rapidly as H_2 molecules transit the PFRC chamber or test cylinder, with molecules having more probability of colliding with a wall or electron than with another molecule or atom. Within the test cylinder, molecules are equally likely to be excited by an electron or collide with the cylinder wall, and electron-impact excitation is three times more likely than collisions with the PFRC chamber wall.

Within the time span of a plasma pulse (3 ms), there are only about 30 inter-molecular and PFRC chamber wall collisions, and about 100 electron-molecule and molecule-test-cylinder-wall collisions. These numbers of collisions are insufficient to equilibrate rotational and translational modes due to the ~ 300 inter-molecular collisions required as discussed previously, and also insufficient to equilibrate vibrational modes with the walls, as will be discussed in the next section. Therefore, no correspondence can be made between the gas temperature and rotational temperature, nor with the vibrational temperature in the PFRC. After the 3 ms plasma pulse, 100 eV electrons are no longer available and the molecules will relax through inter-molecular and wall collisions during the quiescent time (~ 0.3 s) before the next plasma pulse. This is a critical point, since it means the Fulcher-α emission *cannot be used as a gas temperature diagnostic applied to the PFRC*, although could be used in other situations with longer plasma pulse length or greater densities. For example, in typical tokamak vacuum chambers, such as Alcator C-Mod, which have a chamber pressure of $\sim 10^{-3}$ mbar, the room temperature inter-molecular collision time is $\sim 10^{-4}$ s,

Table 3
Characteristic times of the PFRC hydrogen plasma.

Time scale definition	Time (μs)
Steady-state plasma pulse time τ_p	3000
Inter-molecular collision time τ_{coll}	100
PFRC chamber wall collision time $(\tau_{wall})^{PFRC}$	100
Test cylinder wall collision time $(\tau_{wall})^{TEST}$	30
100 eV electron$\rightarrow H_2$ $^3\Pi_u$ excitation collision interval τ_{ex}	30
H_2 (d $^3\Pi \rightarrow$ a $^3\Sigma_g^+$) spontaneous emission time τ_{em}	0.04
H_2 (a $^3\Sigma_g^+$) spontaneous emission time $\tau_2 = 1/A_{21}$	0.01

resulting in ~ 5000 inter-molecular collisions in a 0.5 s plasma pulse. Rotational and translational temperatures should be equilibrated in such tokamak regimes, and thus a gas temperature could be measured using the rotational temperature obtained from the Fulcher-α emission.

4. Ground states of hydrogen

Otorbaev [15] provided the empirical formula that the gas temperature $T_{gas} > 7B/k = 615$ K for the $H_2 \times {}^1\Sigma$ ground state to have a Boltzmann distribution. However, their analysis assumes inter-molecular collisions are frequent enough to have a significant effect. A similar inter-molecular collision argument was used to derive a critical rotational quantum number above which the rotational modes may in non-equilibrium as $N \geq N_{crit} \approx kT_r/4B_v hc + (1/2) \approx 1$ for the H_2 (X $^1\Sigma_g^+$) ground state at the temperatures expected [24,53]. These inter-molecular collision arguments are based on the exponential drop in the concentration of molecules with translational energy sufficient to cause a $|\Delta N| = 2$ transition (neighboring rotational level transitions $|\Delta N| = 1$ are forbidden by symmetry). In kinetic plasmas where inter-molecular collisions are infrequent, these arguments are irrelevant. Other effects, including electron-impact excitation, wall collisions and feed gas rate must instead be considered.

4.1. Effect of wall collisions

The effect of wall collisions on molecular internal energy modes varies depending on wall material, wall temperature, and H_2 translational energy. In the often-cited molecular dynamics (MD) calculations of Hiskes and Karo [54,55], just several wall collisions result in equipartition among the translational, rotational and vibrational modes, with each mode gaining a broad distribution. In their calculations, H_2 with translational energies corresponding to 0.04–0.13 eV, predominantly in the $N=1$ rotational mode, and in excited vibrational states from $\upsilon = 2$ up to 14, impacted Fe wall atoms at an initial temperature of 500 K. In addition to quick equipartition, Hiskes and Karo noted that little energy was lost from H_2 internal modes to the wall. They provide a simple model for vibrational de-excitation as $n_\upsilon \sim \exp[-c/b(\upsilon)]$, where c is the collision number with the wall and $b(\upsilon)$ equals 2.5, 2.0, 1.9, and 1.8 for $\upsilon = 1, 2, 3, 4$, respectively (values up to $\upsilon = 14$ are given in Ref. [54]). Gorse et al. [56] provide a different vibrational deactivation rate equation, $\dot{n}_\upsilon = -n_\upsilon V_{H2} \gamma_\upsilon / 2R$, where γ_υ is the vibrational deactivation coefficient and R is the vacuum chamber vessel radius. They obtained an experimental value for γ_1 of $\sim 10^{-4}$ for a 1.26 cm radius Pyrex tube containing 15 Torr of H_2. Comparing the deactivation rate equation Hiskes and Karo with that of Gorse et al., it is noted that they are equivalent, assuming the wall collision rate is $V_{H2}/2R$, with $b(\upsilon) = 1/\gamma_\upsilon$. Therefore, Gorse et al.'s characteristic number of collisions for vibrational deactivation is $\sim 10^4$ for $\upsilon = 1$, which is significantly higher than 2.5 predicted by Hiskes and Karo.

Capitelli and Gorse [4] showed that H_2 molecules transfer very little energy to Cu wall phonons, citing the relatively small mass of H_2 compared to copper, in agreement with Hiskes and Karo's result that little energy is absorbed by walls. However, contrary to Hiskes and Karo, Capitelli and Gorse found that rotational and vibrational modes were not quenched by wall collisions. Capitelli and Gorse used H_2 pressures of 2.25–15 mTorr and ~ 2 eV electron excitation, and based their results on semi-classical interaction of H_2 molecules with a non-rigid wall where excitation of surface phonons and electrons are treated quantum mechanically, whereas Hiskes and Karo used a classical MD numerical method. Experiments in low-pressure, low electron energy plasmas with stainless steel walls [57–59] also showed that vibrational modes can survive for possibly hundreds of wall collisions, but translational and rotational modes equilibrate much more quickly and on similar time scales. Numerical and experimental studies by Watts et al. [60] found that vibrational de-excitation results in rotational excitation during H_2 collisions with copper walls, and that the survivability of ro-vibrational modes falls substantially with increasing H_2 translational energy (> 0.1 eV).

The numerical results of Cacciatore and Billing [61] using a multi-dimensional semi-classical approach showed that vibrational modes are generally unchanged by collisions with copper walls for H_2 translational energies less than 1.5 eV. Similarly, Hollmann et al. [62,63] found low accommodation coefficients (10^{-2}–10^{-3}) for vibrational and rotational modes in $\sim$mTorr linear diverter experiments of H_2 with a stainless steel wall, and also found that rotational transition probabilities are $\sim 10^{-4}$ per collision, which again runs contrary to the results of Hiskes and Karo. Finally, Wang et al. [64–66] simulated H_2 collisions with Cu walls applying a quantum wave packet model and classical trajectory model, determining that translational-rotational equilibration is efficient at translational energies less than 0.5 eV, the probability of rotational transitions scales as $\exp(-1/T_{\text{wall}})$, and that vibrational excitation is minimal at low translational energies.

In summary, at the low temperatures expected in the PFRC (< 0.1 eV), *rotational* modes likely equilibrate with the wall temperature in several collisions if no non-equilibrating electron-impact collisions occur between subsequent wall collisions. As detailed in Table 3, however, these rates are similar such that a Boltzmann rotational distribution at the wall temperature is still not necessarily justified. Therefore, a detailed analysis of the rotational populations has been done, as will be detailed later. In contrast, *vibrational* modes cannot necessarily be assumed in any particular distribution since hundreds if not thousands of wall collisions may be needed to equilibrate with the wall, and again electron impacts can affect the vibrational populations. The vibrational level populations will thus be left as an unknown in the spectroscopic modeling.

4.2. Ground state vibrational distribution

Due to the previous discussion regarding the overall unknown *a priori* distribution of vibrational population due to collisions of H_2 with walls, electrons and other molecules, the ground state vibrational distribution will be assumed to be in one of three categories: (1) all molecules are effectively in the ground vibrational state ($\upsilon = 0$), which

is valid for temperatures up to ∼1000 K; (2) the vibrational populations follow a Boltzmann distribution at temperature T_v greater than ∼1000 K; or (3) the ground state vibrational populations are arbitrary resulting from the combined effect of the various collision processes within the ground electronic state.

These categories can be incorporated into the relation $n_v = \rho_v \cdot n_{H2}$ for the ground state vibrational populations. For the 1st and 2nd categories, ρ_v is $\exp[-G(v)hc/k_B T_v]/Q_v$ (Q_v is the vibrational partition function) for a Boltzmann distribution. Note that for vibrational equilibrium at temperatures < 1000 K, effectively all the H_2 population is in the $v=0$ state ($\rho_{v=0}=1$; $\rho_{v \neq 0}=0$), corresponding to the 1st category scenario. If wall collisions can be considered to have minimal effect on vibrational modes, then electron-impact excitations within the ground electronic state and secondary processes determine the form of the vibrational populations, which could have an arbitrary distribution (ρ_v is then analogous to excitation Franck–Condon factors). In this 3rd category case, therefore, ρ_v will value between 0 and 1 for each vibrational level v when the vibrational levels are not in equilibrium (and therefore a vibrational temperature is not meaningful).

This unknown *a priori* vibrational population prescription will be used as a means to diagnose the actual ground state distribution implicitly through ratios of the vibrational bands, as will be described later.

4.3. Ground state rotational distribution

A separate analysis was conducted to quantify the ground rotational populations incorporating the combined effects of electron-impact excitation, wall collisions and feed gas rate [67]. This analysis showed that non-equilibrating electron-impact excitation can begin to overwhelm equilibrating wall collisions when their rates are similar, especially for low rotational levels, and that gas feed rate competes with the wall collision rate to determine the rotational temperature for higher rotational levels. Relevant examples from this work of the predicted ground state rotational distributions for the PFRC chamber and test cylinder are shown in Fig. 7a and b, respectively. As seen in Fig. 7a, the N=0, 1, 2 rotational levels are slightly non-Boltzmann, with a rotational temperature of about 505 K, while higher rotational levels asymptote to a Boltzmann distribution at a temperature between the wall and feed gas temperatures.

For the test cylinder modeling shown in Fig. 7b, the N=0, 1, 2 levels are far from Boltzmann, with higher rotational levels following a Boltzmann at the feed gas temperature of ∼300 K. This non-Boltzmann behavior is the result of molecules striking the test cylinder wall only about once during their transit through the tube. This was estimated from Monte Carlo simulations (to be discussed later). Also from the simulation results, the translational temperature was estimated to be ∼225 K. In any case, as described earlier there are not enough inter-molecular collisions during the PFRC plasma pulse to correlate the rotational and translational modes, and rotational modes do not equilibrate within the copper test cylinder.

The nuclear spin degeneracies of the *para* (even N) and *ortho* (odd N) modifications of hydrogen should also be taken into account in the population calculation, since
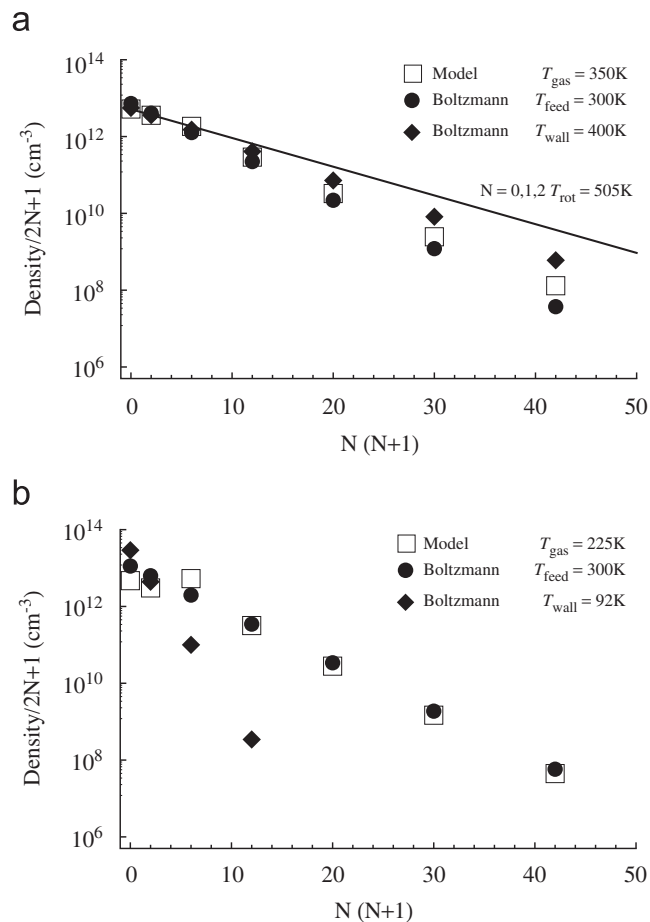

Fig. 7. Boltzmann plots of the ground state rotational distributions accounting for the combined effects of electron-impact excitation, wall collisions and feed gas rate for (a) the PFRC chamber and (b) the test cylinder within the PFRC chamber. Gas feed rate is 4 sccm, and 100 eV electrons at a density of 10^{12} cm^{-3}.

these factors directly affect the observed emission intensities. As discussed previously, the *ortho* modification has total nuclear spin L=1, while *para* has L=0, resulting in a nominal relative degeneracy of 3:1. However, at low temperatures the H_2 molecular population equilibrium tends towards the *para* modification [14,68], as given by the "Hund factor" (the ratio of rotational partition functions) for the equilibrium ratio of *para:ortho* densities as

$$\phi(T) = \frac{\sum_{N=0,2,4,...}(2N+1)\exp[-N(N+1)B_v hc/k_B T]}{\sum_{N=1,3,5,...}(2N+1)\exp[-N(N+1)B_v hc/k_B T]} \quad (13)$$

Eq. (13) was calculated as shown in Fig. 8, where the *para* modification is the most populous modification at low temperatures, and approaches 1/2 at room temperatures and above. However, achieving this low-temperature equilibrium towards the *para* population requires a significant amount of time. For example, at 20 K the time required for the convert half the population to the *para* modification is three years, although addition of charcoal to the system reduces this time to hours [68]. For the PFRC chamber, which is not cooled, consideration of the Hund factor is therefore not needed. For the test cylinder, which is cooled to ∼92 K, and although the interior is coated with a carbon-based graphene material, there is insufficient
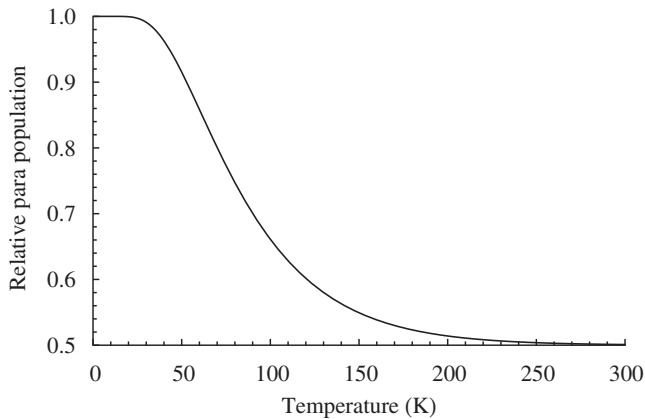
Fig. 8. Relative population of the *para* modification as a function of temperature.

residence time of molecules within the cylinder to cause an adjustment of the relative *para* and *ortho* populations. Therefore, a 50:50 mixture of *para* and *ortho* modification populations will be assumed throughout the PFRC chamber, including within the test cylinder. For other experiments where the chamber is cooled to cryogenic temperatures over a long period of time, especially if carbon-based catalysts are present, the Hund factor may need to be considered. The $(2L+1)$ degeneracy factor must be incorporated into spectral intensity modeling regardless.

For the following analysis, the population density for the ground rotational states will be assumed to be a Boltzmann distribution, and the vibrational distribution as unknown, using

$$n_{\upsilon N} = n_\upsilon (2L+1)(2N+1)\exp\{-B_\upsilon hcN(N+1)/k_B T_r\}/Q_r$$
$$= \rho_\upsilon n_{H2}(2L+1)(2N+1)\exp\{-B_\upsilon hcN(N+1)/k_B T_r\}/Q_r \quad (14)$$

where n_υ is the density of ground vibrational states υ as discussed previously, and Q_r is the rotational partition function, which can be approximated as $kT_r/2B_\upsilon hc$ [69]. Note that the $2S+1$ degeneracy of the ground state equals one, so is not included in Eq. (14).

5. Electron-impact excitation of hydrogen molecules

The excited state ro-vibrational distribution $n_{\upsilon'N'}$ in the $(d\ ^3\Pi_u^-)$ electronic state can be calculated using the coronal approximation similar to Eq. (11) as

$$n_{\upsilon'N'}\left(\frac{1}{\tau_{em}} + \frac{1}{\tau_{quench}}\right) = n_e\sum_{\upsilon,N}n_{\upsilon N}\alpha_{\upsilon N}^{\upsilon'N'} \quad (15)$$

where $\alpha_{\upsilon N}^{\upsilon'N'}$ is the ro-vibronic transition probability from $(\upsilon, N) \rightarrow (\upsilon', N')$ due to electron-impact excitation. The electron excitation cross section will be discussed shortly. Using the time scales of Table 3, the spontaneous emission time dominates over collisional quenching, so τ_{quench} can be neglected [70]. Eq. (15) can thus be written as

$$n_{\upsilon'N'} = \tau_{em}n_e\sum_{\upsilon,N}n_{\upsilon N}\alpha_{\upsilon N}^{\upsilon'N'} \quad (16)$$

With optical selection rules ($\Delta N=0, \pm 1$) for electron-impact excitation, the excitation rate requires a first-rank

spherical scattering tensor as given by

$$(\alpha_{\upsilon N}^{\upsilon'N'})^{dipole} = \langle \sigma_{\upsilon N}^{\upsilon'N'} V_e \rangle$$
$$= q_\upsilon^{\upsilon'}\langle\sigma_0 V_e\rangle(2N'+1)\begin{pmatrix} N' & 1 & N \\ \Lambda' & \Lambda-\Lambda' & -\Lambda \end{pmatrix}^2$$
$$= \langle\sigma_0 V_e\rangle q_\upsilon^{\upsilon'} \quad (17)$$

where σ_0 is the nominal excitation cross section for rotational transitions averaged over a Maxwellian distribution of the electrons of average velocity V_e. The term in braces is the Wigner $3-j$ symbol (equivalent to Clebsch–Gordon angular momentum coupling coefficient), and $q_\upsilon^{\upsilon'}$ is the Franck–Condon factor for vibrational excitation from the υ to υ' states. The $3-j$ symbol of Eq. (17) equals $1/2N'+1$ for the $\Sigma \rightarrow \Pi$ Q-branch excitation [71]. The right side of Eq. (17) also highlights the common assumption that excitation rates are independent of rotational quantum number.

The Born–Oppenheimer approximation has been used above allowing the separation of electronic and nuclear wave functions, which is justified when the ground vibrational state ($\upsilon=0$) wave function's spatial extent ($\sqrt{\hbar/2\pi m_H c\varpi_e} \sim 10^{-9}$ cm) is much smaller than the equilibrium distance between the H_2 nuclei ($\sim 10^{-8}$ cm for H_2), which is approximately valid for H_2 [72].

Lavrov et al. [45] derived a semi-empirical expression for $\alpha_{\upsilon N}^{\upsilon'N'}$ accounting for electron-impact transitions that do not necessarily follow the Franck–Condon approximation by using the r-centroid method [73] and Morse potential vibrational wave functions [74]. For even rotational transitions ($\Delta N=0, \pm 2$) their semi-empirical excitation rate is

$$(\alpha_{\upsilon N}^{\upsilon'N'})^{Lavrov} = \langle\sigma_0 V_e\rangle(2N'+1)\left\{G_{\upsilon\upsilon'}^{(1)}\begin{pmatrix} N' & 1 & N \\ 1 & -1 & 0 \end{pmatrix}^2\right.$$
$$\left. +G_{\upsilon\upsilon'}^{(2)}\begin{pmatrix} N' & 2 & N \\ 1 & -1 & 0 \end{pmatrix}^2\right\} \quad (18)$$

where $G_{\upsilon\upsilon'}^{(1)}$ and $G_{\upsilon\upsilon'}^{(2)}$ are the vibrational mode-dependent weights of first-rank and second-rank spherical tensors, respectively. Since the Franck–Condon (FC) approximation was not assumed, the excitation cross section depends on the combined ro-vibrational transition, but $G_{\upsilon\upsilon'}^{(1)}$ can be considered analogous to excitation Franck–Condon factors. From the results of Lavrov et al. [45], σ_0 at ~ 100 eV is $\sim 3 \times 10^{-18}$ cm², and the vibrationally dependent excitation factors are reproduced in Table 4.

Otorbaev et al. [15] derived a rotational excitation cross section similar to Lavrov et al. [45], but averaged over vibrational bands for the weighting factors up 4th-rank

Table 4
First- and second-rank spherical tensor vibrational weights $G_{\upsilon\upsilon'}^{(1)}$ and $G_{\upsilon\upsilon'}^{(2)}$. Negligible quantities (< 0.001) represented with dashes.

υ	$G_{\upsilon\upsilon'}^{(1)}$				$G_{\upsilon\upsilon'}^{(2)}$			
	$\upsilon'=0$	1	2	3	$\upsilon'=0$	1	2	3
0	0.012	0.021	0.028	0.032	0.0019	0.0022	0.0014	–
1	0.057	0.021	0.002	–	0.009	0.004	–	–
2	0.14	–	0.017	0.014	0.017	–	0.0027	0.0025
3	0.168	0.092	0.035	–	0.015	0.009	0.005	–

Lavrov et al. [45].

Table 5
Relative values of $\sigma_N^{N'}$ for rotational excitation of the levels d $^3\Pi_u$, normalized to σ_0^1 and averaged over vibrational bands.

N	N'=1	2	3	4	5
0	1.00	0.16	0.13	0.02	$< 10^{-4}$
1	0.55	0.58	0.10	0.07	0.01
2	0.17	0.54	0.45	0.09	0.06
3	0.04	0.19	0.53	0.41	0.08
4	0.01	0.05	0.22	0.53	0.38
5	10^{-3}	0.02	0.05	0.23	0.53

spherical tensors as

$$\left(\alpha_{\upsilon N}^{\upsilon' N'}\right)^{Otorbaev} = q_\upsilon^{\upsilon'} \sigma_N^{N'} = q_\upsilon^{\upsilon'} \langle \sigma_0 V_e \rangle (2N'+1) \sum_{r=1}^{4} \overline{G}^{(r)} \begin{pmatrix} N' & r & N \\ 1 & -1 & 0 \end{pmatrix}^2 \tag{19}$$

where $\overline{G}^{(r)}$ is the partial electron cross section for direct electron excitation involving change in molecular electron spin, averaged over vibrational levels, for each multi-pole of rank r. Here, the Franck–Condon approximation was assumed. For the X $^1\Sigma_g^+ \rightarrow$ d $^3\Pi_u$ excitation, empirical values for $\overline{G}^{(r)}$ averaged over electron current densities of 1–20 mA/cm^2 were empirically determined to be $\overline{G}^{(r)}$={0.76, 0.122, 0.1, 0.014}. Note that $\overline{G}^{(2)}$ and $\overline{G}^{(3)}$ are accurate to 30–40%, and $\overline{G}^{(4)}$ within a factor of 2. However, these values reproduced Otorbaev's multiple experimental results well since the main contribution to $\sigma_N^{N'}$ is from the $\overline{G}^{(1)} = 0.76$ term, which has higher accuracy.

Using the empirically determined $\overline{G}^{(r)}$ values in Eq. (19), the relative rotational excitation cross sections can be calculated, as given in Table 5. From Table 5 it can be seen that $|\Delta N| > 1$ transitions do not populate the upper state rotational levels as effectively as $|\Delta N| \le 1$ transitions, conforming to the Bryukhovetskiy [31] approximate selection rule $|\Delta N| \le |\Lambda' - \Lambda| = 1$. Also, note that the $\Delta N = 0$ transition probabilities are all approximately equal. However, $|\Delta N| > 1$ excitation probabilities are non-zero, and not necessarily negligible for $\Delta N = \pm 2$ (i.e. quadrupole excitation).

Using the ground state distribution of ro-vibrational populations as given by Eq. (14) along with the electron-impact excitation models incorporated in Eqs. (16)–(19), the upper state distributions can be calculated for the three cases: (1) purely dipole-allowed excitation (optical selection rules) and assuming the FC approximation; (2) Non-optical selection rules (dipole and quadrupole excitation) and assuming the FC approximation (hereafter called the Otorbaev model); and (3) Non-optical selection rules and not assuming the FC approximation (Lavrov model). With the upper state ro-vibrational populations estimated, emission intensities can then be calculated.

6. Results

The above equations were incorporated into the numerical software package *Mathematica* in matrix form to efficiently solve for the upper state rotational and vibrational populations. The excitation and emission Franck–Condon factors of Fantz and Wunderlich [75] were used, which include fifteen vibrational levels and utilized the best Born–Oppenheimer potential curves and electric dipole transition moments available. The emission FC factors of Fantz and Wunderlich compare well with the results of Spindler [74]. Although up to fifteen vibrational ground states can be included (υ=0–14), for applicable vibrational temperatures (up to 9000 K) only the υ=0–3 levels are appreciably populated. However, to analyze the effect of non-Boltzmann vibrational distributions, higher vibrational levels can be populated so the FC factors for large vibrational levels can be useful. Boltzmann vibrational, or arbitrary distributions, are implemented into the code and are easily adjusted.

Spectral measurements were made by attaching the spectrometer system optical fiber to a viewing port of the PFRC (see Figs. 4 and 9) to view either the interior of the FRC region of the plasma, or within the cryogenically cooled copper test cylinder (see Fig. 5). The test cylinder data was obtained with the wall temperature held near 92 K. Data from the cooled copper cylinder were to be used to provide a data point at a gas temperature below that of the experiment of Fantz and Heger [76] ($\sim$450 K), and above the cryogenic temperature of Otorbaev et al. [22] ($\sim$160 K). To estimate the gas temperature within the cooled copper cylinder, and average number of collisions a H$_2$ molecules makes within the cylinder walls, The Monte Carlo neutral transport code DEGAS 2 was used [77]. The code takes as input the device geometry, background plasma density and temperature, as well as the strength and location of the gas puff source of H$_2$. An absorbing surface mocks up the effect of an external pump. The neutral–plasma and neutral–neutral interactions incorporated into these simulations are described in Stotler et al. [78], and include multi-step ionization of H, neutral molecule and molecular ion dissociation, and elastic scattering. The code provides on output the atomic and molecular densities and temperatures everywhere in the volume. A wall accommodation coefficient of 0.36 [79] was used in the simulations for translational modes of H$_2$ equilibrating with carbon-based wall material. From these numerical simulations, the H$_2$ gas temperature within the copper cylinder is estimated to be $\sim$225 K. An average H$_2$ molecule collides with the cylinder interior wall about once during its transit, such that full wall accommodation does not occur for rotational modes.

Unfortunately, not enough collisions of H$_2$ molecules occurred within the test cylinder to justify a rotational temperature, as was shown in Fig. 7b, so this data cannot be used. The data obtained from the PFRC might have been useable, but as shown in Fig. 7a, the actual rotational temperature could be between room temperature and $\sim$500 K, such that the data of Fantz and Heger [76] are better to use for comparison to modeling.

6.1. Upper vibrational state populations

Shown in Fig. 10 are upper state vibrational populations of the υ=0, 1, 2, and 3 levels obtained from measured vibrational bands of Fantz and Heger [76] and in the present study. Fantz and Heger used either a 90% H$_2$ and 10% He gas mixture (Fig. 10a) or 10% H$_2$/90% He gas mixture
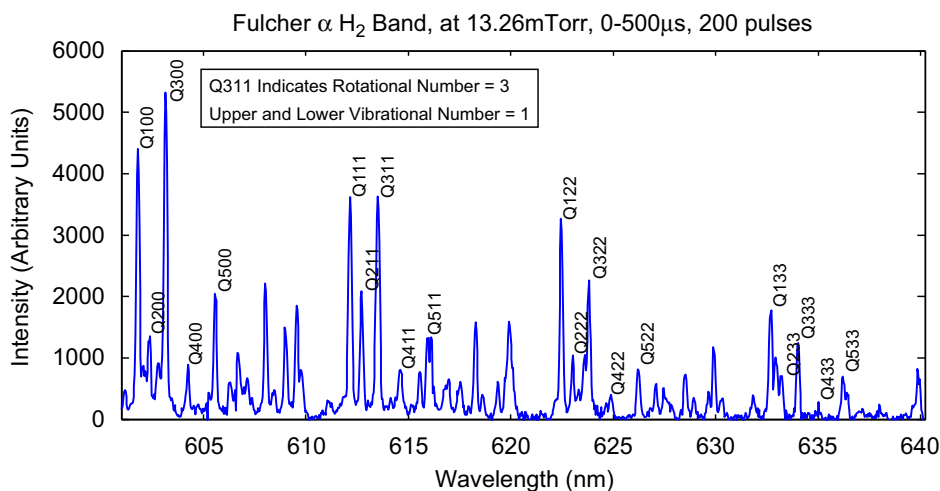
Fig. 9. Fulcher-α spectra taken with the PFRC at 13.26 mTorr using the 600 groove/mm grating.

(Fig. 10b). The helium was useful as a separate gas temperature diagnostic, which provided an estimate of $T_{gas} \sim 450$ K for their experiments. Their pressures were low at 30–135 mTorr, and impacting electron energies were 2–5 eV at a density of 9×10^{10} cm^{-3} measured through microwave interferometry. The upper state populations were estimated by taking recorded vibrational band emission intensities and dividing through by the emission branching ratios of Fantz and Heger (see their Table 2). Data from the present experiments are shown in Fig. 10c.

The three models for electron-impact excitation were run assuming a Boltzmann vibrational distribution is applicable for the ground states, and the associated vibrational temperature iterated to achieve a best fit with the measurements. The models produce relatively high vibrational temperatures from ~3500 to 6800 K. As can be seen from all the plots, the model of Lavrov, which did not assume the FC approximation, do not match well with experimental data, whereas the dipole and Otorbaev models match quite well. Note that for vibrational levels, the dipole and Otorbaev models produce the same results since both assume the FC approximation and use the same FC factors. The dipole/Otorbaev models are not as accurate for the $\upsilon = 3$ level, but the trend line for increasing vibrational levels is clear. It is also interesting to note that the present experiments, conducted at 1–2 orders of magnitude lower pressure and 2 orders of magnitude greater electron energy and density, are in-line with similar *relative* vibrational level populations obtained by Fantz and Heger. This is to be expected when the FC and Born–Oppenheimer approximations are valid since under these assumptions the vibrational excitation and emission rates should not depend on impacting electron characteristics (i.e. the vibrational populations depend only on the overlap integrals of the vibrational wave functions for upper and lower states).

These results indicate that the Franck–Condon approximation is appropriate, and that the ground state vibrational distribution is Boltzmann. Fantz and Heger [76] came to the same conclusion. Many runs of the Lavrov model were done, from room temperature to 9000 K, and

with non-Boltzmann distributions (e.g. all ground vibrational levels equally populated, or higher populated tails than Boltzmann), but the Lavrov model could not be adjusted to fit the data. Since the primary motivation for Lavrov et al. [45] producing their model was due to their doubts as to the applicability of the FC approximation, the fact that their model does not match experimental vibrational data puts their model in doubt. Although the Lavrov model likely is not applicable, it will continue to be explored for rotational line intensities in the next section.

6.2. Intensities of Fulcher-α ro-vibronic emissions

The photon emission rate of a ro-vibronic line in defined as

$$I(\upsilon',\upsilon'';N',N'') = n_{\upsilon'N'}A(\Lambda',\Lambda'';\upsilon',\upsilon'';N',N'') \quad (20)$$

The Einstein emission coefficient A, normalized by rotational state degeneracy, is given by [14,71,75]

$$A(\Lambda',\Lambda'';\upsilon',\upsilon'';N',N'') = \frac{64\pi^4\bar{\nu}^3}{3h(4\pi\varepsilon_0)}\left|R(\Lambda',\Lambda'';\upsilon',\upsilon'';N',N'')\right|^2/(2N'+1) \quad (21)$$

where ε_0 is the permittivity of free space, $\bar{\nu}_{N'}$ is the wavenumber of the emission line, and $|R(\Lambda',\Lambda'';\upsilon',\upsilon''; N',N'')|^2$ is the square of the electric dipole transition moment including electronic, vibration and rotation effects. Using the Born–Oppenheimer approximation to separate the electronic and nuclear wave functions, the dipole moment can be divided into separate electronic, vibrational and rotational parts as [80]

$$\left|R(\Lambda',\Lambda'';\upsilon',\upsilon'';N',N'')\right|^2 = \bar{R}_e^2(\Lambda',\Lambda'') \cdot q_{\upsilon''}^{\upsilon'} \cdot S(\Lambda',\Lambda'';N',N'') \quad (22)$$

where $\bar{R}_e^2$ is the adiabatic electronic transition probability (square of the electric dipole transition moment), $q_{\upsilon''}^{\upsilon'}$ is the emission FC factor, and $S(N', N'')$ is the line strength, or Hönl–London factor, for rotational transitions. This separation of the electronic and nuclear motions is justified for the diagonal vibrational bands, although the electronic transition probability does depend slightly on the

a

b

c
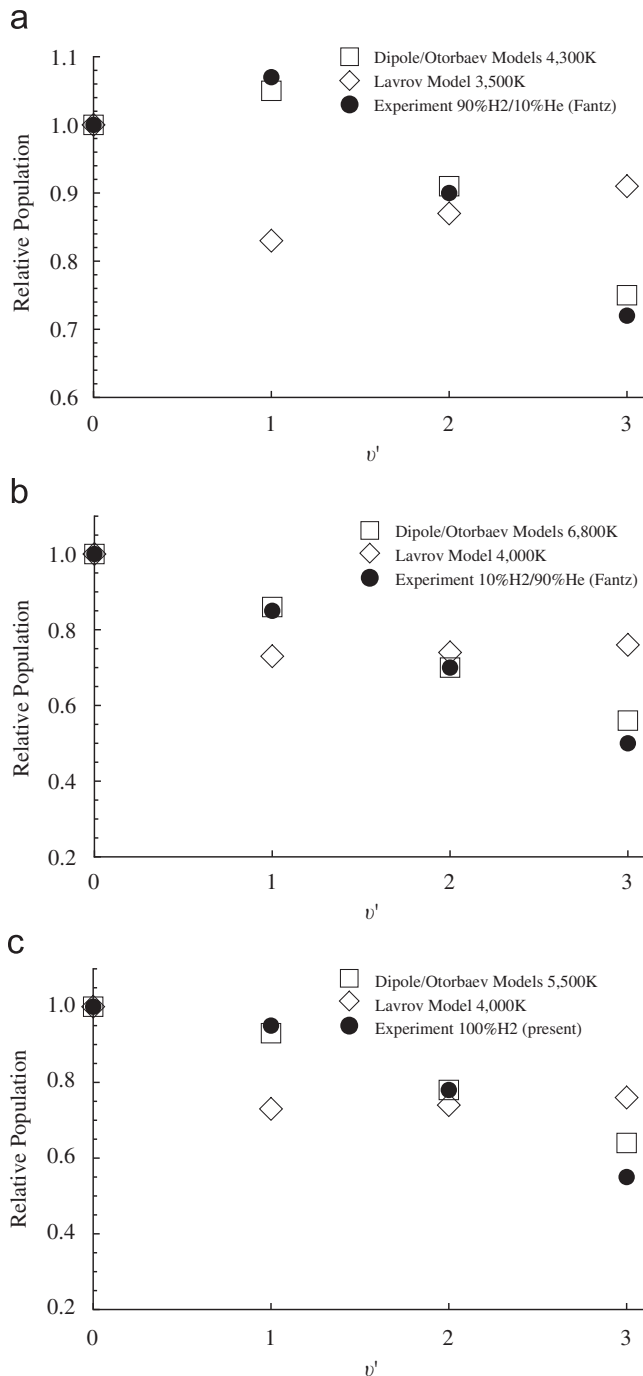
Fig. 10. Distribution of upper state vibrational populations comparing experimental data and dipole, Otorbaev and Lavrov excitation models. Data normalized by the (0,0) band intensity: (a) Fantz and Heger [76] data for a 90% hydrogen, 10% He mixture; (b) Fantz and Heger [76] data for a 10% hydrogen, 90% He mixture; and (c) present experimental data.

inter-molecular distance [81] such that the Born–Oppenheimer approximation can break down for the Fulcher-α emission, in particular for non-diagonal bands [82]. Therefore, for non-diagonal bands the electronic transition probability $\overline{R}_e^2$ and FC factor $q_{v''}^{v'}$ should not be separated, and the actual total emission rates tabulated by Fantz and Wunderlich [75] should instead be used. Using the Fantz and Wunderlich tables of spontaneous emission rates and FC factors, the electronic dipole transition

moment for emission from the Fulcher-α diagonal bands (through $v'=v''=3$) is obtained as $|R_e|=1.89$ a.u. (1.42×10^{-29} C m), which corresponds well with the results of Staszewska and Wolniewicz (not surprising since Fantz and Wunderlich used the transition moments of Staszewska and Wolniewicz in their analysis) [78].

The Hönl–London factor is given by [71]

$$S(\Lambda',\Lambda'';N',N'') = (1+\delta_{\Lambda'0}+\delta_{\Lambda''0}-2\delta_{\Lambda'0}\delta_{\Lambda''0})$$

$$\times (2N'+1)(2N''+1)\begin{pmatrix} N' & 1 & N'' \\ -\Lambda' & \Lambda'-\Lambda'' & \Lambda'' \end{pmatrix}^2 \tag{23}$$

which for the Q-branch transitions of the Fulcher-α emission ($\Lambda'=1$, $\Lambda''=0$) equals ($2N'+1$). Using this Hönl–London factor with Eqs. (20)–(22), the intensity of a Q-branch ro-vibronic line is

$$I(v',v'';N') = \frac{64\pi^4 \overline{\nu}^3}{3h(4\pi\varepsilon_0)} n_{v'N'} \overline{R}_e^2 \cdot q_{v''}^{v'} \tag{24}$$

The upper state population, Eq. (16), is calculated from the ground state population, Eq. (14), and the various electron-impact excitation models of Eqs. (17)–(19). These results are shown in Fig. 11 for the $N'=1\rightarrow 5$ ro-vibronic lines of the Fulcher-α emission. Lower intensity lines for $N' > 5$ would also be visible at the higher temperatures in Fig. 11, but are not shown to avoid clutter.

As depicted in Fig. 11, the intensity of the Q-branch $N'=1$ line is strong for temperatures of interest (up to 1000 K), and the $N'=3$ line intensity as calculated with the Lavrov model is about 30% higher than that of the dipole and Otorbaev models. The intensity of the $N'=2$ line in both the Otorbaev and Lavrov models remains elevated at low temperatures, in contrast to the $N'=2$ line of the dipole model which tends towards zero. The $N'=2$ line does not go to zero in the Otorbaev and Lavrov models because the quadrupole contribution to the excitation rate asymptotes to a non-zero constant as the temperature approaches zero. All of the models produce line intensities which follow similar general trends due to the assumption of a Boltzmann ground state rotational distribution.

To illustrate the differences in the models and compare with data, line ratios of the $N'=2$ and 3 intensities normalized by the $N'=1$ line are shown in Fig. 12a and b, respectively. The data from Otorbaev et al. [22] was measured in 0.5 Torr hydrogen discharge plasma with an electron energy of several eV, and obtained separate gas temperature measurement of 160 ± 25 K from spectral line widths. The vertical error bars for the Otorbaev data were estimated directly from their published intensity uncertainties. The data of Fantz and Heger [76] were measured in 90% hydrogen, 10% helium mixture electron-cyclotron-heated plasma at pressures of 30–135 mTorr and several eV electron energy. Small amounts of nitrogen were added to obtain a separate gas temperature measurement of 450 ± 50 K. Vertical error bars for the Fantz and Heger data were estimated from inspection of their published sample spectra.

Clearly the Lavrov model does not follow the rotational line data. Combined with the previous problem of the Lavrov model not matching vibrational band data, the conclusion is made that the Lavrov model is not appropriate,
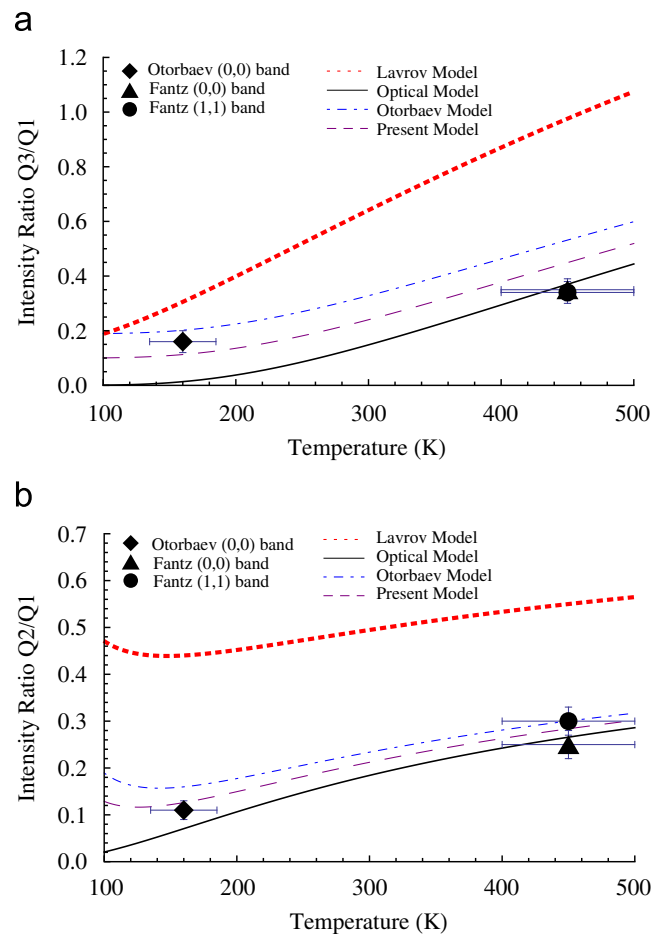
a

b

c
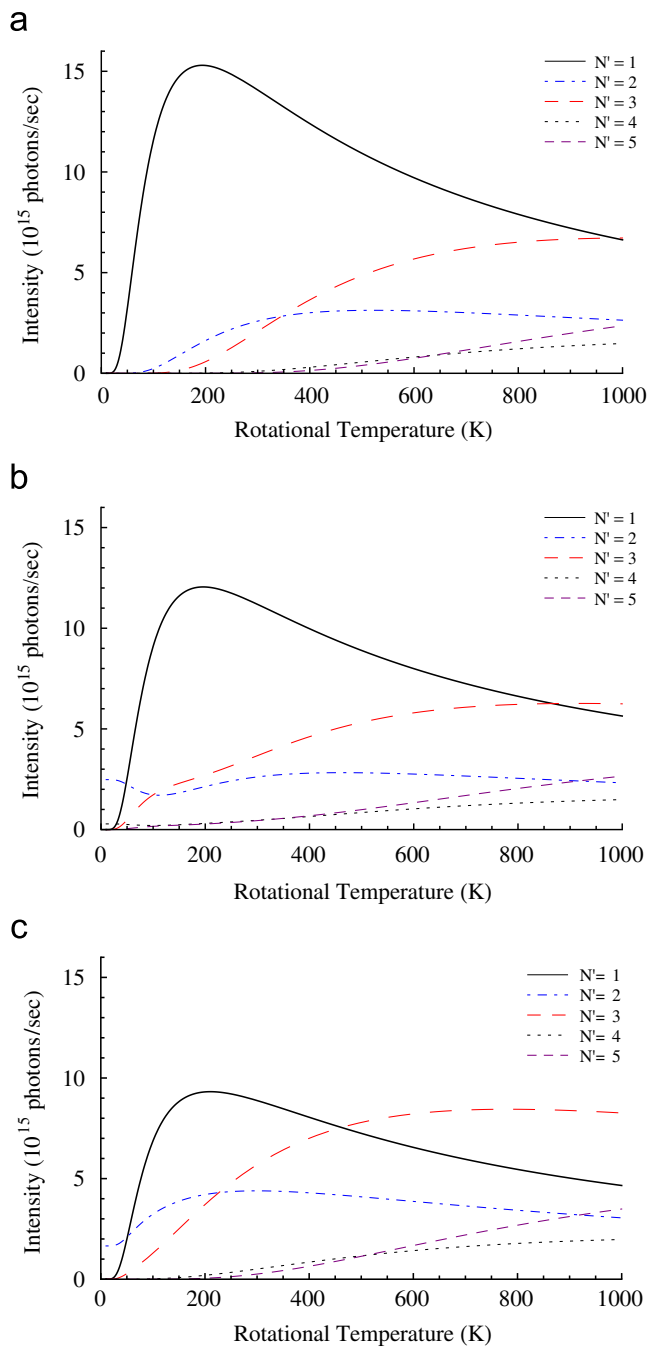
Fig. 11. Intensities of the $N'=1\to5$ rotational lines versus rotational temperature for: (a) the dipole, optical selection rules model; (b) the Otorbaev model using non-optical selection rules and the Franck–Condon approximation; and (c) the Lavrov model using non-optical selection rules and no Franck–Condon approximation.

a

b

Fig. 12. Comparison of electron-impact excitation models for rotational line intensities: (a) intensity ratios of the Q3/Q1 rotational lines and (b) intensity ratios of the Q2/Q1 rotational lines.

implicitly confirming that the FC approximation is valid. The Lavrov model will therefore not be considered further, and the FC approximation assumed.

The rotational line data appear to lie between the dipole and Otorbaev models, and the relatively large error bars do not allow a conclusion to be made as to which model is better. Also, neither model matches best at both low and high temperatures. As such, a simplified dipole-quadrupole model was developed, depicted as the "present model" in Fig. 12. This model is similar to the Otorbaev model, but

rather than include multi-poles up to $r=4$ (allowing $\Delta N=0$, ±2, ±4), we only include the dipole and quadrupole contributions (allowing $\Delta N=0$, ±2), and leave the relative weight of the quadrupole contribution as an adjustable parameter. In this case, the exact algebraic solution for the upper state population is given by

$$n_{v'N'} = \frac{\tau_{em}n_e n_{H2}\sum_v\rho_v q_v^{v'}}{Q_r}(2L+1)(2N'+1)$$
$$\times\exp\left[-B_vhcN'(N'+1)/k_B\theta_r\right]\left\{1+\gamma X(N')\right\}$$
where
$$X(N') = \frac{3}{(2N'+3)(2N'-1)} + \frac{2(N'-1)(N'+1)}{(2N'+1)(2N'-1)}$$
$$\times\exp\left[2B_vhc(2N'-1)/k_B\theta_r\right]$$
$$+ \frac{2N'(N'+2)}{(2N'+1)(2N'+3)}\exp\left[-2B_vhc(2N'+3)/k_B\theta_r\right]$$

(25)

Here, γ is the adjustable weighting of the quadrupole contribution, and θ_r represents a quasi-rotational temperature. Note that the *ground state* rotational constant B_v is maintained, while the upper state rotational quantum number N' is used since $N=N'$ for Q-branch transitions. The $\Delta N=\pm2$ quadrupole transitions are incorporated into $X(N')$. This avoids complications such as using an

"excitation temperature" as discussed previously. If quadrupole contributions are needed, then by definition the resulting rotational distribution is non-Boltzmann and therefore the concept of temperature loses its meaning. Note that when $\gamma = 0$, the dipole model is recovered and $\theta_r \equiv T_r$. In Fig. 12, γ was set to 0.1, and as can be seen the fit of this simpler dipole-quadrupole model with the data is better than that of the purely dipole or Otorbaev multi-pole models.

Since the intensities of the $N' = 1, 2, 3$ lines will have the highest signal-to-noise at temperatures below 1000 K and represent over 70% of the hydrogen molecules, fitting of these lines is most important in determining the rotational temperature. As can be estimated from Fig. 12, the dipole and Otorbaev models applied to measured spectral data would result in temperatures differing by ~ 100–150 K. If this level of error is acceptable, then any of the models above, with the exception of the Lavrov model, could be used. Again, if quadrupole excitation is needed, then γ is not zero and the concept of a rotational temperature must be used with care.

The relative effect of the quadrupole contribution to the excitation rate is given by $\gamma X/(1+\gamma X)$, as illustrated in Fig. 13. Quadrupole excitation is relatively small at all temperatures for the $N' = 1$ level since the 2nd term in the relation for $X(N')$ in Eq. (25) becomes zero and the 3rd term is small at all temperatures. The $N' > 1$ levels, however, have significant contributions from quadrupole excitation at lower temperatures. As expected, increasing γ increases the quadrupole effect accordingly. However, while the quadrupole contribution can be significant for individual lines, the effect is not as dramatic when looking at line ratios, or Boltzmann plots, which depend only on the relative line strengths, since the quadrupole-related increases in intensity cancel out to great extent. This damping of the rather strong quadrupole effect expected for room temperatures of the $N' = 1, 2, 3$ lines is illustrated in Fig. 12, where the difference from purely dipole modeling is not significant.

Rotational lines within a vibrational band can be summed to calculate the diagonal band strengths, as shown in Fig. 14. Boltzmann distributions are assumed for the ground vibrational levels, corresponding to $T_v = 0 \rightarrow 9000$ K (labels "1" to "9" in Fig. 14). Note that for vibrational temperatures at or below about 1000 K, all the population is in the $v = 0$ level, such that the "1" label actually corresponds to all temperatures between 0 and 1000 K. As can be seen from Fig. 14, the data of Fantz and Heger [76] as well as the present data fit within the Boltzmann assumption. From inspection of Fig. 14, our vibrational temperature is between 5000 and 6000 K. The (3,3) band modeling was not as accurate as the (1,1) and (2,2) bands, as was identified in Fig. 10, so the temperatures obtained from fits with the (1,1) and (2,2) bands have more weight.

Also shown in Fig. 14 is the resulting band intensities for non-Boltzmann distributions $\rho_v = \{1, 1/2, 1/4, 0\}$ (labeled "linear"), and a flat-top distribution $\rho_v = \{1, 1, 1, \ldots\}$ for all vibrational levels up to $v = 14$. The "linear" distribution lies below the Boltzmann region in Fig. 14, and the flat-top distribution runs contrary to the trend lines for Boltzmann distributions. Thus, Fig. 14 can be used as a convenient
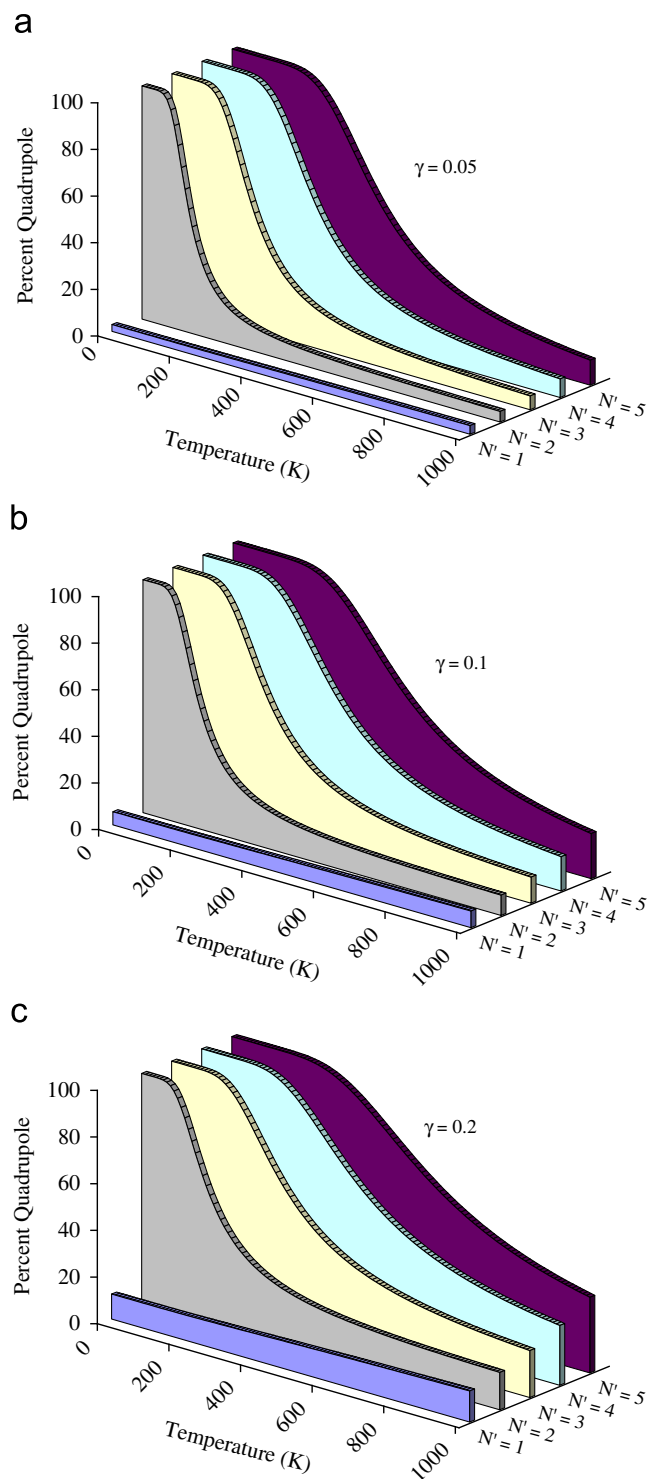
Fig. 13. Relative contribution of quadrupole excitation to dipole excitation for: (a) $\gamma = 0.05$; (b) $\gamma = 0.1$; and (c) $\gamma = 0.2$.

means to quickly estimate the vibrational temperature from an experiment, if the bands intensities fall within the trends of the Boltzmann region of Fig. 14, which then provides directly the ground state vibrational populations. If one's measured band intensities do not follow the Boltzmann trend lines of Fig. 14, then the ground vibrational distribution can be deemed non-Boltzmann, and depending on how the data lie on the plot and estimation of the ground
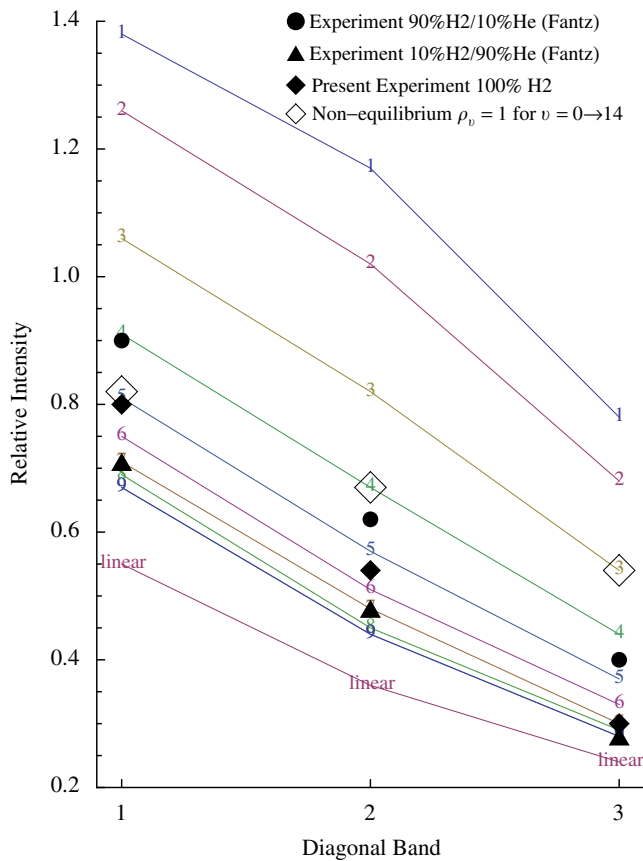
Fig. 14. Relative vibrational band strengths for the (1,1), (2,2) and (3,3) bands normalized by the (0,0) strength. The listed numbers correspond to thousands of Kelvin (e.g. "2"=2000 K). "Linear" refers to $\rho_v=\{1,1/2,1/4,0\}$. Fantz data from [76].

state vibrational populations could be inferred. In such a non-Boltzmann case, the ρ_v can be iterated using the present model until a reasonable fit with data is achieved, giving the ground state vibrational level distribution.

7. Summary

The PFRC plasma was shown to be in the kinetic regime, and optically thin to the Fulcher-α emission (d $^3\Pi_u \rightarrow$ a $^3\Sigma_g^+$) between 600 and 640 nm. A time scale analysis showed that inter-molecular collisions are rather infrequent, and due to the large number of collisions required to equilibrate hydrogen's rotational and translational modes ($\sim$300), no correlation can be made between the gas temperature and rotational temperature. Radiative emission occurs much more rapidly than hydrogen collisions with electrons or wall structures. A test cylinder inserted within the PFRC vacuum vessel fixed a cold wall temperature on the modeling of the rotational ground state, but not enough wall collisions occur to equilibrate the rotational modes. This unfortunate result should be a caution to the reader to be sure rotational equilibrium assumptions are valid before reporting rotational temperatures.

Quantum mechanical selection rules for *ortho* and *para* modifications of hydrogen were followed, illustrating that even rotational transitions ($\Delta N=0, \pm 2, \pm 4,...$) during electron-impact excitation cause Q-branch emissions only. Non-optical selection rules are possible at low

electron-impact energies (below several hundred eV) due to a violation of the 1st Born approximation. The Born–Oppenheimer and Franck–Condon approximations appear to hold, and consequently the excitation model of Lavrov et al. [45] is not appropriate. The Lavrov model also did not follow experimental vibrational band and rotational line intensities. The so-called Hund factor quantifying the relative equilibrium populations of *ortho* and *para* modifications is not needed for the PFRC or test cylinder analyses since the cold temperatures experienced by the hydrogen molecules is brief, but this factor should be considered in low temperature scenarios where the molecules have ample time to adjust for bath temperatures below $\sim$150 K.

Relative diagonal vibrational band intensities show that the PFRC has a vibrational temperature of 5000–6000 K, with a corresponding Boltzmann ground state vibrational distribution. Since the PFRC wall temperature is at approximately room temperature, the wall accommodation coefficient for vibrational modes of hydrogen is very low. The PFRC is operated in a 1% duty cycle, so hydrogen molecules will experience thousands of wall collisions during the quiescent periods ($\sim$300 ms) between plasma pulses, yet maintain a high vibrational temperature. However, inter-molecular collisions during the quiescent period are sufficient to achieve a Boltzmann vibrational distribution. This confirms the results of several authors that excited vibrational levels can be maintained through hundreds to thousands of wall collisions [56–66], and that the results of Hiskes and Karo [54,55], where vibrational modes decay within just several wall collisions, is not correct.

Fig. 14 provides a quick visual means to estimate hydrogen vibrational temperatures through relative vibrational band intensities. If measured band strengths do not follow the Boltzmann trend lines, then the ground vibrational populations are likely not Boltzmann. In such cases, the ground state vibrational distribution can be determined through iteration of the function ρ_v in the spectroscopic model. Fig. 14 is valid within the accuracy of the excitation and emission Franck–Condon factors of Fantz and Wunderlich [75] (which adhere to the results of Staszewska and Wolniewicz [78] and Spindler [74]), and the Born–Oppenheimer and Franck–Condon approximations.

The dipole-quadrupole model of Eq. (25) provides a means to quantify a quasi-rotational temperature θ_r and the quadrupole contribution to rotational line intensities. This spectroscopic model, which includes the possibility of non-optical excitation transitions, is simpler than the model of Otorbaev et al. [15], and leaves the quadrupole contribution as an adjustable parameter γ. Measured ro-vibronic line data can be fit roughly by varying θ_r in Eq. (25), and the quadrupole contribution γ adjusted to fine tune the fit with the data. If quadrupole excitation is not needed (e.g. the iterated γ is negligibly small), then optical (dipole) selection rules are only needed, and the rotational ground state can be assumed Boltzmann such that a rotational temperature can be rigorously defined ($\theta_r \equiv T_r$). Optical selection rules are expected for relatively large electron impact energies (greater than several hundred eV) where the 1st Born approximation is valid. As depicted in Fig. 13, quadrupole contributions are most significant at lower

temperatures, though the effect somewhat cancels when dealing with relative intensities in a Boltzmann plot or rotational line ratios. Using the dipole-quadrupole model with $\gamma = 0.1$ (10% quadrupole contribution) achieved the best fit with the lower temperature data of Otorbaev et al. [15] and higher temperature data of Fantz and Heger [76]. However, the large horizontal error bars representing the associated temperature uncertainties make it difficult to confirm whether quadrupole excitation is truly needed, and hence we cannot with certainty determine whether non-optical or optical selection rules are appropriate.

The present dipole-quadrupole spectroscopic model for the Fulcher-α Q-branch emission assumes the Born–Oppenheimer and Franck–Condon approximations, but not necessarily the 1st Born approximation. For non-optical selection rules, care must be taken in using a rotational temperature since in such a case the distribution is necessarily non-Boltzmann to some degree. For kinetic hydrogen plasmas, the ground rotational populations may not be fully Boltzmann, such as for the PFRC, in which case the actual distribution of levels should be used in Eq. (14) and carried through to Eq. (25). For *collisional* hydrogen plasmas, a Boltzmann ground state rotational distribution given by Eq. (14) is appropriate, and the excitation analysis conducted herein is unaltered.

Acknowledgments

References

[1] Cohen SA, Berlinger B, Brunkhorst C, Brooks A, Ferraro N, Lundberg DP, et al. Formation of collisionless high-β plasmas by odd-parity rotating magnetic fields. Phys Rev Lett 2007;98:072508.

[2] Brunkhorst C, Berlinger B, Ferraro N, Cohen SA The Princeton FRC rotating-magnetic-field-experiment RF system. In: Proceedings of the 22nd IEEE/NPSS symposium on fusion engineering—SOFE 07, Piscataway, NJ: Institute of Electrical and Electronics Engineers Inc; 2007, Article No. 4337897.

[3] Ohno N, Ezumi N, Takamura S, Krasheninnikov SI, Pigarov AYu. Experimental evidence of molecular activated recombination in detached recombining plasmas. Phys Rev Lett 1998;27:818–21.

[4] Capitelli M, Gorse C. Open problems in the physics of volume H$^-$/D$^-$ sources. IEEE Trans Plasma Sci 2005;33:1832–44.

[5] Fukumasa O, Saeki S. Effect of wall material on negative ion production in a hydrogen plasma. J Phys D: Appl Phys 1987;20:237–40.

[6] Hiskes JR, Karo AM. Generation of negative ions in tandem high-density hydrogen discharges. J Appl Phys 1984;56:1927–38.

[7] Hassouni K, Gicquel A, Capitelli M, Loureiro J. Chemical kinetics and energy transfer in moderate pressure H$_2$ plasmas used in diamond MPACVD processes. Plasma Sources Sci Tech 1999;8:494–512.

[8] Krstić PS, Schultz DR, Janev RK. Charge transfer processes in slow collisions of protons with vibrationally excited hydrogen molecules. Phys Scr 2002;96:61–71.

[9] De Graaf MJ, Severens R, Dahiya RP, Van de Sanden MCM, Schram DC. Anomalous fast recombination in hydrogen plasmas involving rovibrational excitation. Phys Rev E 1993;48:2098–102.

[10] Chapman S, Cowling TG. The mathematical theory of non-uniform gases. New York: Cambridge University Press; 1970 p. 246.

[11] Cottrell TL, McCoubrey JC. Molecular energy transfer in gases. London: Butterworth; 1961 p. 78.

[12] Born M. Quantenmechanik der Stossvorgnge (Quantum mechanics of impact processes). Z Phys 1926;38:803–27.

[13] Yamasaki D, Kado S, Xiao B, Iida Y, Kajita S, Tanaka S. Experimental evaluation of predissociation rate in $v = 4$ state usable for analysis of H$_2$ Fulcher-α band emission. J Phys Soc Japan 2006;75:044501.

[14] Herzberg G. Molecular spectra and molecular structure I. Spectra of diatomic molecules. New York: Van Nostrand; 1955.

[15] Otorbaev DK, Ochkin VN, Rubin PL, SYu Savinov, Sobolev NN, Tskhai SN. Electron-impact excitation levels of the rotational levels of molecular electron states in gas discharges. In: Sobolev NN, editor. Electron-excited molecules in non-equilibrium plasma. New York: Nova Science Publishers Inc; 1989. p. 121–73.

[16] Ginsburg N, Dieke GH. Intensity measurements in the molecular spectrum of hydrogen. Phys Rev 1941;59:632–44.

[17] De Graaf MJ, Qing Z, Van Roojj G, Van de Sanden MCM, Heeren RMA, Kleyn AW. Rotational and gas temperatures in a surface conversion negative ion source. AIP Conf Proc 1994;287:588–94.

[18] Kado S, Yamasaki D, Xiao B, Iida Y, Okamoto A, Kajita S, et al. On the anomalous characteristics in the P and R branches in a hydrogen Fulcher band. J Plasma Fusion Res Series 2006;**7**:54–8.

[19] Richardson OW. Molecular hydrogen and its spectrum. New Haven: Yale University Press; 1934 p. 178.

[20] Kovács I. Rotational structure in the spectra of diatomic molecules. London: Adam Hilger; 1966.

[21] Dieke GH. Triplet 3p complex of the hydrogen molecule. Phys Rev 1935;48:610–4.

[22] Otorbaev DK, Ochkin VN, SYu Savinov, Sobolev NN, Tskhai SN. Transfer of appreciable angular momentum in electron excitation of molecules. JETP Lett 1978;28:392–6.

[23] Lavrov BP, Ostrovskii VN, Ustimov VI. Determination of the gas temperatures of a low-pressure plasma from the intensities of the H$_2$ and D$_2$ molecular bands; rotational transitions under electron-impact excitation. Opt Spectrosc 1979;47:30–4.

[24] Lavrov BP, Ostrovskii VN, Ustimov VI. Mechanism for production of nonequilibrium rotational level populations of molecules in plasma. I. Theoretical model. Sov Phys Tech Phys 1980;25:1208–13;
Lavrov BP, Ostrovskii VN, Ustimov VI. Mechanism for production of nonequilibrium rotational level populations of molecules in plasma. II. Comparison with experiment. Sov Phys Tech Phys 1980;25:1213–6.

[25] Lavrov BP, Solov'ev AA, Tyutchev MV. Populations of the rotational levels of the d $^3\Pi_u^-$ levels of H$_2$, HD, and D$_2$ in an RF discharge. J Appl Spectrosc 1980;32:316–20.

[26] Lavrov BP. Determination of the gas temperature of a low-pressure plasma from the intensities of the H$_2$ and D$_2$ molecular bands. Relationship between the intensity distribution in a band and the gas temperature. Opt Spectrosc 1980;48:375–80.

[27] Lavrov BP, Ostrovskii VN, Ustimov VI. Cross sections and rate constants for the electron-impact excitation of electronic-rotational molecular states. Sov Tech Phys Lett 1979;5:142–4.

[28] Lavrov BP, Ostrovskii VN, Ustimov VI. Rotational transitions in the excitation of electronic states of molecules by electron impact. Sov Phys JETP 1979;49:772–6.

[29] Qing Z, Otorbaev DK, Brussaard GJH, Van de Sanden MCM, Schram DC. Diagnostics of the magnetized low-pressure hydrogen plasma jet: molecular regime. J Appl Phys 1996;80:1312–24.

[30] Shikama T, Kado S, Zushi H, Tanaka S. Molecular Zeeman spectroscopy for H$_2$ Fulcher-α band spectra as a local measurement of rovibrational structures. Phys Plasmas 2007;14:072509.

[31] Bryukhovetskiy AP, Kotlikov EN, Otorbaev DK, Ochkin VN, Rubin PL, SYu Savinov, et al. Excitation of electron-vibrational-rotational levels of hydrogen molecules by electron impact in a nonequilibrium gas-discharge plasma. Sov Phys JETP 1980;52:852–60.

[32] Mott NF, Massey HSW. The theory of atomic collisions. 3rd ed.. New York: Oxford University Press; 1987 p. 328, 458.

[33] Oppenheimer JR. On the quantum theory of electronic impacts. Phys Rev 1928;32:361–76.

[34] Trajmar S, Cartwright DC, Rice JK, Brinkmann RT, Kuppermann A. Angular dependence of low-energy electron-impact excitation cross section of the lowest triplet states of H$_2$. J Chem Phys 1968;49:5464–72.

[35] Bates DR, Fundaminsky A, Leech JW, Massey HSW. Excitation and ionization of atoms by electron impact—The Born and Oppenheimer approximations. Trans Royal Soc 1950;A243:93–143.

[36] Born M, Oppenheimer R. Quantum theory of molecules. Ann Phys 1927;84:457–84;
Born M, Oppenheimer R. Quantum theory of molecules. In: Hettema H, editor. Quantum chemistry. Classic Scientific Papers, Singapore: World Scientific Publishing Ltd; 2000. p. 1–20 English version.

[37] Green AES, Stolarski RS. Analytic models of electron impact excitation cross sections. J Atmos Terr Phys 1972;34:1703–17.

[38] Lassettre EN, Symposium G. Elementary physical processes. Rad Res Suppl 1959;1:530–46.

[39] Muntz E.P. The electron beam fluorescence technique. NATO AGAR-Dograph 132 1968.

[40] Farley DR, Cattolica RJ. Electron beam fluorescence from the A $^2\Pi$–X $^2\Pi$ and B $^2\Sigma^+$–X $^2\Pi$ transitions of CO_2^+. JQSRT 1996;56:83–96.

[41] Shimada M, Cattolica R, Tynan GR. Electron beam fluorescence temperature measurements of N_2 in a semiconductor plasma reactor. J Vac Sci Technol A 2004;22:371–6.

[42] Villarejo D, Stockbauer R, Ingham MG. Vibration-rotation interaction effects in calculated Franck–Condon factor II. Hydrogen Lyman and Fulcher bands. J Chem Phys 1969;50:1754–62.

[43] Hutchinson IH. Principles of plasma diagnostics. 2nd ed.. New York: Cambridge University Press; 2002 p. 225–45.

[44] Baltayan P, Nedelec O. Relative intensities and polarizations in H_2 rotational lines excited by electron impact. J Phys 1975;36:125–33.

[45] Lavrov BP, Ostrovsky VN, Ustimov VI. Non-Franck–Condon transitions in the electron impact excitation of molecules II. Semi-empirical approach: transitions in H_2. J Phys B: At Mol Phys 1981;14:4701–18.

[46] Astashkevich SA, Lavrov BP. Lifetimes of the electronic-vibrational-rotational states of hydrogen molecule (review). Opt Spectrosc 2002;92:818–50.

[47] Khakoo MA, Trajmar S. Electron-impact excitation of the a $^3\Sigma_g^+$, B $^1\Sigma_u^+$, c $^3\Pi_u$, and C $^1\Pi_u$ states of H_2. Phys Rev A 1986;34:146–56.

[48] Tawara H, Itikawa Y, Nishimura H, Yoshino M. Cross sections and related data for electron collisions with hydrogen molecules and molecular ions. J Phys Chem Ref Data 1990;19:617–36.

[49] Smith WH, Chevalier R. Radiative-lifetime studies of the emission continua of the hydrogen and deuterium molecules. Astrophys J 1972;177:835–9.

[50] King GC, Read FH, Imhof RE. The measurement of molecular lifetimes by the photon–photon delayed coincidence method. J Phys B 1975;8:665–73.

[51] Griem HR. Plasma spectroscopy. New York: McGraw-Hill; 1964 p. 197.

[52] Lide DR, editor. CRC handbook of chemistry and physics. 85th ed.. Roca Baton: CRC Press; 2005.

[53] Astashkevich SA, Käning M, Käning E, Kokina NV, Lavrov BP, Ohl A, et al. Radiative characteristics of $3p \Sigma, \Pi$; $3d \Pi^-, \Delta^-$ states of H_2 and determination of gas temperature of low pressure hydrogen containing plasmas. JQSRT 1996;56:725–51.

[54] Hiskes JR, Karo AM. Analysis of the H_2 vibrational distribution in a hydrogen discharge. Appl Phys Lett 1989;54:508–10.

[55] Karo AM, Hiskes JR, Hardy RJ. Vibrational relaxation in H_2 molecules by wall collisions: applications to negative ion source processes. J Vac Sci Technol A 1985;3:1222–8.

[56] Gorse C, Capitelli M, Ricard A. On the coupling of electron and vibrational energy distributions in H_2, N_2, and CO post discharges. J Chem Phys 1985;82:1900–6.

[57] Stutzin GC, Young AT, Schlachter AS, Leung KN, Kunkel WB. In situ measurement of rovibrational populations of H_2 ground electronic state in a plasma by VUV laser absorption. Chem Phys Lett 1989;155:475–80.

[58] Eenshuistra PJ, Bonnie JHM, Los J, Hopman HJ. Observation of exceptionally high vibrational excitation of hydrogen molecules formed by wall recombination. Phys Rev Lett 1988;60:341–4.

[59] Hall RI, Cadez I, Landau M, Pichou F, Schermann C. Vibrational excitation of hydrogen via recombinative desorption of atomic hydrogen gas on a metal surface. Phys Rev Lett 1988;60:337–40.

[60] Watts E, Sitz GO, McCormack DA, Kroes GJ, Olsen RA, Groeneveld JA, et al. Rovibrationally inelastic scattering of $(v=1, j=1)$ H_2 from Cu(100): experiment and theory. J Chem Phys 2001;114:495–503.

[61] Cacciatore M, Billing GD. Dissociation and atom recombination of H_2 and D_2 on metallic surfaces: a theoretical survey. Pure Appl Chem 1996;68:1075–81.

[62] Hollmann EM, AYu Pigarov, Yan Z. Measurement of cross-field power loss due to rovibrationally excited H_2 in a detached hydrogen diverter plasma simulator. Phys Plasmas 2006;13:052510.

[63] Hollmann EM, AYu Pigarov, Taylor K. Measurement and modeling of hydrogen vibrational and rotational temperatures in weakly-ionized hydrogen discharges. J Nucl Mat 2005;337–339:451–5.

[64] Wang ZS, Darling GR, Holloway S. Translation-to-rotational energy transfer in scattering of H_2 molecules from Cu(1 1 1) surfaces. Surf Sci 2000;458:63–70.

[65] Wang ZS, Darling GR, Holloway S. Surface temperature dependence of the inelastic scattering of hydrogen molecules from metal surfaces. Phys Rev Lett 2001;87:226102.

[66] Wang ZS, Darling GR, Holloway S. Vibration-rotational coupling of H_2 molecules scattering from a Cu(1 1 1) surface. Surf Sci 2002;504:66–74.

[67] Farley DR. Calculation of ground state rotational populations for kinetic gas homonuclear diatomic molecules including electron-impact excitation and wall collisions. J Chem Phys 2010;133:094303.

[68] Kennard EH. Kinetic theory of gases. New York: McGraw-Hill Book Company; 1938 p. 262–4.

[69] McQuarrie DA, Simon JD. Molecular thermodynamics. Sausalito: University Science Books; 1999 p. 152–9.

[70] Burshstein ML, Lavrov BP, Melnikov AS, Prosikhin VP, Yurgenson SV, Yakovlev VN. Measurement of the radiative lifetimes and collisional-quenching rate coefficients for the H_2-molecule d $^3\Pi_u^-$, v, N levels. Opt Spectrosc 1990;68:166–8.

[71] Hansson A, Watson JKG. A comment on Hönl–London factors. J Mol Spectrosc 2005;233:169–73.

[72] Cohen-Tannoudji C, Diu B, Laloe F. Quantum mechanics. Singapore: John Wiley & Sons; 2005 p. 505–14.

[73] Lavrov BP, Ostrovsky VN, Ustimov VI. Non-Franck–Condon transitions in the electron impact excitation of molecules I. Theory. J Phys B: At Mol Phys 1981;14:4389–97.

[74] Spindler RJ. Franck–Condon factors for band systems of molecular hydrogen—I. JQSRT 1969;9:597–626.

[75] Fantz U, Wunderlich D. Franck–Condon factors, transition probabilities, and radiative lifetimes for hydrogen molecules and their isotopomeres. At Data Nucl Data Tables 2006;92:853–973.

[76] Fantz U, Heger B. Spectroscopic diagnostics of the vibrational population in the ground state of H_2 and D_2 molecules. Plasma Phys Control Fusion 1998;40:2023–32.

[77] Stotler DP, Karney CFF. Neutral gas transport modeling with DEGAS 2. Contrib Plasma Phys 1994;34:392–7.

[78] Stotler DP, Pitcher CS, Boswell CJ, Chung TK, LaBombard B, Lipschultz B, et al. Effect of baffling on diverter leakage in ALCATOR C-mod. J Nucl Mater 2001;290–293:812–9.

[79] Yasumoto I. Accommodation coefficients of helium, neon, argon, hydrogen, and deuterium on graphitized carbon. J Phys Chem 1987;91:4298–301.

[80] Zare RN. Angular momentum. New York: John Wiley & Sons; 1988 p. 283–6.

[81] Staszewska G, Wolniewicz L. Transition moments among $^3\Sigma$ and $^3\Pi$ states of the H_2 molecule. J Mol Spectrosc 1999;198:416–20.

[82] Kirbyateva TV, Lavrov BP, Ostrovskii VN, Tyutchev MV, Ustimov VI. Probabilities of the d $^3\Pi_u^- \to$ a $^3\Sigma_g^+$ radiative transitions in the hydrogen molecule. Opt Spectrosc 1982;52:21–6.